



# The ubiquitin ligase UBE3B, disrupted in intellectual disability and absent speech, regulates metabolic pathways by targeting BCKDK

Solmi Cheon<sup>a</sup>, Kiran Kaur<sup>a</sup>, Nadine Nijem<sup>a</sup>, Islam Oguz Tuncay<sup>b</sup>, Pooja Kumar<sup>a</sup>, Milan Dean<sup>a</sup>, Jane Juusola<sup>c</sup>, Maria J. Guillen-Sacoto<sup>c</sup>, Emma Bedoukian<sup>d</sup>, Lynne Ierardi-Curto<sup>e</sup>, Paige Kaplan<sup>e</sup>, G. Bradley Schaefer<sup>f</sup>, Prashant Mishra<sup>g</sup>, and Maria H. Chahrouh<sup>a,b,h,1</sup>

<sup>a</sup>Eugene McDermott Center for Human Growth and Development, University of Texas Southwestern Medical Center, Dallas, TX 75390; <sup>b</sup>Department of Neuroscience, University of Texas Southwestern Medical Center, Dallas, TX 75390; <sup>c</sup>GeneDx Inc., Gaithersburg, MD 20877; <sup>d</sup>Roberts Individualized Medical Genetics Center, Children's Hospital of Philadelphia, Philadelphia, PA 19104; <sup>e</sup>Division of Human Genetics and the Metabolic Disease Program, Children's Hospital of Philadelphia, Philadelphia, PA 19104; <sup>f</sup>Division of Genetics, University of Arkansas for Medical Sciences, Little Rock, AR 72205; <sup>g</sup>Children's Medical Center Research Institute, University of Texas Southwestern Medical Center, Dallas, TX 75390; and <sup>h</sup>Department of Psychiatry, University of Texas Southwestern Medical Center, Dallas, TX 75390

Edited by Arthur L. Beaudet, Baylor College of Medicine, Houston, TX, and approved January 4, 2019 (received for review October 31, 2018)

**Kaufman oculocerebrofacial syndrome (KOS) is a recessive neurodevelopmental disorder characterized by intellectual disability and lack of speech. KOS is caused by inactivating mutations in UBE3B, but the underlying biological mechanisms are completely unknown. We found that loss of Ube3b in mice resulted in growth retardation, decreased grip strength, and loss of vocalization. The brains of Ube3b<sup>-/-</sup> mice had hypoplasia of the corpus callosum, enlarged ventricles, and decreased thickness of the somatosensory cortex. Ube3b<sup>-/-</sup> cortical neurons had abnormal dendritic morphology and synapses. We identified 22 UBE3B interactors and found that branched-chain  $\alpha$ -ketoacid dehydrogenase kinase (BCKDK) is an in vivo UBE3B substrate. Since BCKDK targets several metabolic pathways, we profiled plasma and cortical metabolomes from Ube3b<sup>-/-</sup> mice. Nucleotide metabolism and the tricarboxylic acid cycle were among the pathways perturbed. Substrate-induced mitochondrial respiration was reduced in skeletal muscle but not in liver of Ube3b<sup>-/-</sup> mice. To assess the relevance of these findings to humans, we identified three KOS patients who had compound heterozygous UBE3B mutations. We discovered changes in metabolites from similar pathways in plasma from these patients. Collectively, our results implicate a disease mechanism in KOS, suggest that it is a metabolic encephalomyopathy, and provide an entry to targeted therapies.**

UBE3B gives rise to neurodevelopmental phenotypes, the disease mechanisms in KOS, and the specific substrates of UBE3B that mediate these mechanisms are not known. To address these questions, we sought to investigate the neurobehavioral consequences of losing UBE3B and identify its substrates.

## Results

### Ube3b Knockout Mice Have Growth Retardation and Absent Vocalization.

To understand the physiological function of UBE3B and investigate the mechanisms responsible for the phenotypes seen in KOS, we generated *Ube3b*<sup>-/-</sup> mice (*SI Appendix, Fig. S1*). *Ube3b*<sup>-/-</sup> mice were born in expected Mendelian ratios (*SI Appendix, Fig. S1D*), and had a ~30% reduction in body weight and a ~10% reduction in length compared with control littermates (*Fig. 1A*). In addition, the weights of brain and testes were reduced in *Ube3b*<sup>-/-</sup> mice, while the ratios of organ to body weight were unchanged (*SI Appendix, Fig. S2*). Heterozygous *Ube3b*<sup>+/-</sup> mice were indistinguishable from wild-type (WT) littermates.

Given the complete lack of speech seen in the majority of KOS patients—~89%, including the three patients reported

intellectual disability | autism spectrum disorder | ubiquitination | BCKDK | UBE3B

Neurodevelopmental disorders (NDDs) affect ~15% of children in the United States and pose significant societal and economic burdens (1–4). NDDs make up a clinically and genetically heterogeneous group of diseases that affect brain development and function and often other organs. Intellectual disability (ID) and autism spectrum disorder (ASD) are the most common forms of NDD (3, 5) and often coexist in the same individual. The two conditions have high heritability (6, 7), with a multitude of gene defects underlying disease (8–13). Kaufman oculocerebrofacial syndrome (KOS; MIM 244450) is an NDD characterized by severe ID, absence of speech, microcephaly, muscle hypotonia, and growth retardation (14). KOS is an autosomal recessive disorder caused by complete loss-of-function mutations in *UBE3B*, a gene encoding an uncharacterized HECT (homologous to E6AP carboxyl terminus) E3 ubiquitin ligase (14–19). Moreover, we identified a recessive missense *UBE3B* mutation in a family with ASD (20).

UBE3B is a member of the proteasome pathway that functions in protein turnover and ubiquitin-mediated signaling. Mutations in several ubiquitin ligases result in ID and/or ASD, including *UBE3A* in Angelman syndrome (21), *HUWE1* in syndromic X-linked ID (22), *PSMD12* in ID (23), and *UBE3C*, which has recently been associated with ASD risk (24). How disruption of

## Significance

UBE3B is a ubiquitin ligase disrupted in severe neurodevelopmental diseases (NDDs). Mechanistic studies on the function of UBE3B and its substrates have been lacking. Here, we show that deletion of *Ube3b* in mice causes neuroanatomical, behavioral, and metabolic abnormalities. Moreover, we identify BCKDK as a substrate UBE3B ubiquitinates. BCKDK is mutated in a spectrum of NDDs, and encodes a kinase that regulates several metabolic pathways. We show that UBE3B mutations are associated with metabolic disturbances in plasma from patients. Our findings place two NDD genes, UBE3B and BCKDK, in the same pathway, functionally validate the role of UBE3B in human disease, and identify both a disease mechanism in patients with UBE3B mutations and the downstream substrate that mediates this mechanism.

Author contributions: P.M. and M.H.C. designed research; S.C., K.K., N.N., I.O.T., P. Kaplan, M.D., J.J., M.J.G.-S., E.B., L.I.-C., P. Kaplan, G.B.S., P.M., and M.H.C. performed research; S.C., K.K., N.N., I.O.T., P. Kaplan, M.D., P.M., and M.H.C. analyzed data; M.H.C. wrote the paper; J.J., M.J.G.-S., E.B., and G.B.S. referred subjects; and L.I.-C., P. Kaplan, and G.B.S. performed clinical phenotyping of subjects.

The authors declare no conflict of interest.

This article is a PNAS Direct Submission.

Published under the PNAS license.

<sup>1</sup>To whom correspondence should be addressed. Email: maria.chahrouh@utsouthwestern.edu.

This article contains supporting information online at [www.pnas.org/lookup/suppl/doi:10.1073/pnas.1818751116/-DCSupplemental](http://www.pnas.org/lookup/suppl/doi:10.1073/pnas.1818751116/-DCSupplemental).

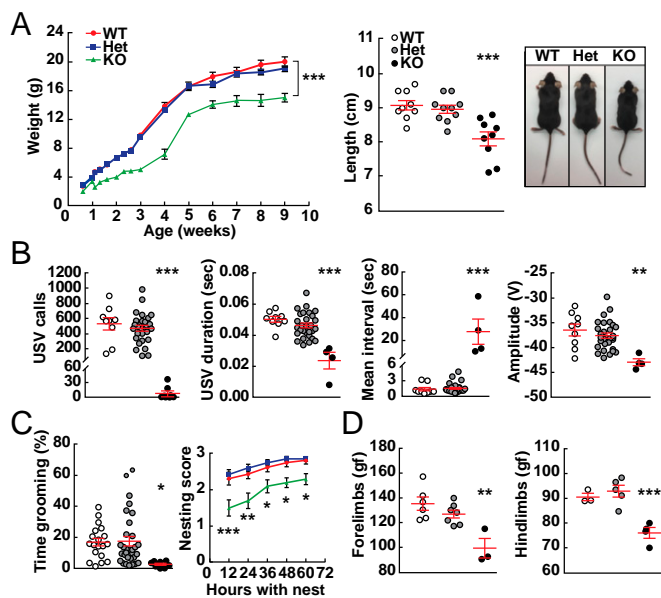


**Fig. 1.** Loss of *Ube3b* results in growth retardation, lack of vocalization, and muscle weakness. (A) *Ube3b*<sup>-/-</sup> knockout (KO) mice show significant reduction in weight and length versus WT or *Ube3b*<sup>+/-</sup> (heterozygotes; Het) (weight: \*\*\**P* < 0.0001, two-way ANOVA; *n* = 5–18 WT, 7–37 Het, 5–12 KO; nose-to-rump length: \*\*\**P* = 0.0003, one-way ANOVA; *n* = 9 WT, 10 Het, 9 KO). (B) KO mice have severe reduction in the number of and changes in duration, interval, and amplitude of USVs (\*\*\**P* < 0.0001, \*\**P* < 0.0025; *n* = 9 WT, 29 Het, 8 KO; duration, interval, amplitude: *n* = 9 WT, 29 Het, 4 KO). (C) KO mice spend less time grooming and their ability to construct nests is impaired (grooming: \**P* = 0.0273; nest building: \*\*\**P* < 0.0005, \*\**P* < 0.002, \**P* < 0.05; *n* = 16–19 WT, 28–31 Het, 8–10 KO). (D) KO mice have reduced grip strength of both forelimbs and hindlimbs (\*\*\**P* = 0.0008, \*\**P* = 0.0019; *n* = 3–6 WT, 5–7 Het, 3–4 KO). Values are mean ± SEM.

here (17)—we analyzed the ability of *Ube3b*<sup>-/-</sup> mice to emit ultrasonic vocalizations (USVs). Almost all *Ube3b*<sup>-/-</sup> mice had complete loss of USVs (Fig. 1B). The few mice that did vocalize had significantly fewer USVs and USV quality was altered compared with control littermates (Fig. 1B and *SI Appendix*, Fig. S3A and B).

We measured self-grooming and marble burying to assess repetitive behaviors and found that *Ube3b*<sup>-/-</sup> mice performed significantly worse than control littermates in both assays (Fig. 1C and *SI Appendix*, Fig. S3C). The *Ube3b*<sup>-/-</sup> mice also performed poorly on the nest building test (Fig. 1C). Since patients with KOS have muscle hypotonia (14), we measured grip strength. We found that *Ube3b*<sup>-/-</sup> mice had reduced muscle strength in both their forelimbs and hindlimbs (Fig. 1D).

**Loss of *Ube3b* Results in Dendritic and Synaptic Abnormalities.** Human and mouse *Ube3b* is expressed ubiquitously, with the highest expression in testis (*SI Appendix*, Fig. S4). The targeted locus in *Ube3b*<sup>+/-</sup> mice included a lacZ cassette enabling us to characterize *Ube3b* expression by β-gal staining. We found that *Ube3b* expression in brain was highest in the hippocampus and cortical layers II/III and V (*SI Appendix*, Fig. S5), which are regions important in cognition and memory. The brains of *Ube3b*<sup>-/-</sup> mice had a hypoplastic corpus callosum and enlarged ventricles (*SI Appendix*, Fig. S6). In addition, the thickness of the primary somatosensory cortex was decreased, while the thickness of the primary motor cortex was preserved (*SI Appendix*, Fig. S6).

To assess the role of *Ube3b* in neuronal development, we measured dendritic complexity, length, and spine density in vivo by Golgi-Cox staining of brains from *Ube3b*<sup>-/-</sup> and WT littermates. Sholl analysis revealed reduced dendritic complexity in cortical neurons from *Ube3b*<sup>-/-</sup> mice (Fig. 2A–C), which was

more pronounced in the caudal cortex (Fig. 2A–C). Cortical neurons from *Ube3b*<sup>-/-</sup> mice had significant reduction in dendritic length (~34–42% decrease) and dendritic spine density (~28–31% decrease) compared with neurons from WT littermates (Fig. 2B and C).

We isolated primary neurons from the cortices of *Ube3b*<sup>-/-</sup> mice and WT littermates. We transfected the neurons with a GFP-expressing plasmid to outline neuronal morphology and immunostained them with presynaptic (synapsin I), postsynaptic [postsynaptic density protein 95 (PSD95)], and inhibitory synapse [vesicular GABA transporter (VGAT)] markers. Cortical neurons from *Ube3b*<sup>-/-</sup> mice had a ~24% decrease in presynaptic (synapsin I) puncta, a ~33% increase in postsynaptic (PSD95) puncta (Fig. 2D), and a ~50% increase in VGAT puncta (Fig. 2E). Collectively, these results suggest a role for UBE3B in neuronal morphogenesis and differentiation.

**Proteomics Identifies UBE3B Interactors.** To identify proteins that physically interact with UBE3B and are candidate substrates, we generated a HEK293T cell line (HEK293T<sup>UBE3B-HA</sup>) that stably expresses a tagged version of UBE3B (UBE3B-HA). This was required since no anti-UBE3B antibodies were available that were suitable for immunoprecipitation. We immunoprecipitated UBE3B-HA and performed mass spectrometry (MS) to detect its interactors. Spectral counts for unique proteins identified by

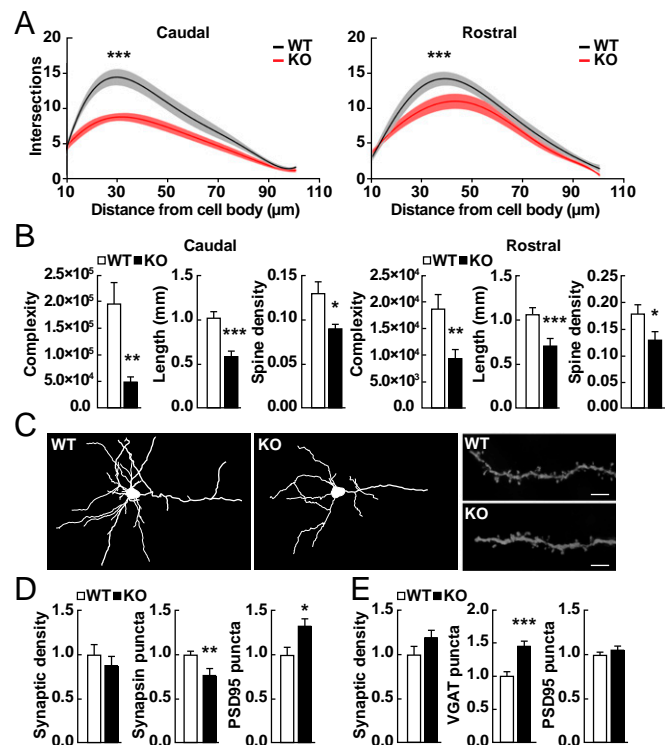


**Fig. 2.** *Ube3b* knockout mice have impaired dendritic morphogenesis and altered synapses. (A) Sholl analysis from Golgi-Cox-stained neurons reveals a reduction in dendritic complexity of cortical neurons from KO versus WT (\*\*\**P* < 0.0001, two-way ANOVA; *n* = 13–15 WT, 10–15 KO). (B) Golgi-Cox staining shows significantly reduced dendritic complexity, length, and spine density in neurons from the caudal and rostral cortex of KO versus WT. Data were obtained from basal dendrites of cortical layer II/III neurons (caudal: \**P* = 0.0235, \*\**P* = 0.0029, \*\*\**P* < 0.0001; rostral: \**P* = 0.0355, \*\**P* = 0.0057, \*\*\**P* = 0.0029; *n* = 13–15 WT, 10–15 KO). (C, Left) Representative tracings of Golgi-Cox-stained cortical layer II/III neurons and (C, Right) of their dendritic segments. (Scale bars, 5 μm.) (D) Primary cortical neurons from KO have less synapsin I puncta and more PSD95 puncta versus WT (\**P* = 0.0213, \*\**P* = 0.004; *n* = 20 WT, 10 KO). (E) Primary cortical neurons from KO have increased VGAT puncta versus WT (\*\*\**P* = 0.0002; *n* = 10 WT, 20 KO).

MS were analyzed using the Comparative Proteomic Analysis Software Suite (CompPASS) as previously described (25). We identified 22 high-confidence candidate interacting proteins (HCIPs) (Table 1). Three of the HCIPs—BCKDK, BCKDHA, and DBT—function in BCAA metabolism (Fig. 3A). The second step in BCAA metabolism catalyzed by the branched-chain  $\alpha$ -ketoacid dehydrogenase complex (BCKDC) is irreversible and rate limiting (26). BCKDC has three components: (i) branched-chain  $\alpha$ -ketoacid decarboxylase, a heterotetramer of two branched-chain  $\alpha$ -ketoacid dehydrogenase E1 alpha (BCKDHA) and two beta (BCKDHB) subunits, (ii) dihydrolipoamide branched-chain transacylase (DBT), and (iii) dihydrolipoamide dehydrogenase (DLD) (Fig. 3A). Thus, we found that two of the three catalytic subunits of BCKDC interact with UBE3B. BCKDK, another HCIP, is the kinase that regulates activity of the complex by phosphorylating and inactivating BCKDHA. Mutations in *BCKDK* cause ID, ASD, and epilepsy (27), while mutations in *BCKDHA* or *DBT* cause maple syrup urine disease (MSUD; MIM 248600), a disorder characterized by ID, developmental delay, and a maple syrup odor to urine (28).

We confirmed that BCKDK and DBT physically interact with UBE3B using coimmunoprecipitation in HEK293T<sup>UBE3B-HA</sup> (SI Appendix, Fig. S7B). To determine whether UBE3B ubiquitinates BCKDK, BCKDHA, or DBT, we performed denaturing immunoprecipitation. We transfected Myc-BCKDK into HEK293T<sup>UBE3B-HA</sup> and into HEK293T cells that do not express UBE3B. We then immunoprecipitated Myc-BCKDK to isolate it without any interacting proteins and performed Western blot analysis with both anti-Myc and anti-ubiquitin antibodies. BCKDK was ubiquitinated in cells expressing UBE3B (Fig. 3B) and this ubiquitination was enhanced by treatment with the proteasome

inhibitor bortezomib (Fig. 3B). Using the same assay in HEK293T<sup>UBE3B-HA</sup> cells and WT tissue, we did not detect ubiquitination of BCKDHA or DBT (SI Appendix, Fig. S8A–C). The data suggest that UBE3B ubiquitinates BCKDK but not BCKDHA or DBT.

**BCKDK Is an In Vivo Substrate of UBE3B.** *Ube3b* is expressed in three tissues that are the major sites of BCAA metabolism: brain, liver, and skeletal muscle (SI Appendix, Figs. S1, S4, and S5). To determine the effect of inactivating *Ube3b* on levels of BCKDK, BCKDHA, and DBT in these tissues, we compared levels of these proteins in *Ube3b*<sup>−/−</sup> mice and control littermates. BCKDK levels were significantly higher in all three tissues of *Ube3b*<sup>−/−</sup> mice (Fig. 3C), which is consistent with BCKDK being an in vivo substrate of Ube3b. In contrast, no differences were seen in the levels of BCKDHA in tissues from *Ube3b*<sup>−/−</sup> mice. DBT levels were increased in skeletal muscle but not cortex or liver of *Ube3b*<sup>−/−</sup> mice (Fig. 3C).

To confirm that changes in BCKDK protein levels were due to a difference in posttranslational modification, we compared *Bckdk* transcript levels in tissues from *Ube3b*<sup>−/−</sup> mice and control littermates. We found no differences in *Bckdk* mRNA levels between genotypes (SI Appendix, Fig. S8D), whereas *Dbt* transcript levels were higher in *Ube3b*<sup>−/−</sup> skeletal muscle (SI Appendix, Fig. S8D). Thus, the observed increase in DBT protein levels (Fig. 3C) was due to transcriptional changes in *Dbt* expression.

**UBE3B Regulates Several Metabolic Pathways.** Since BCKDK phosphorylates key enzymes in several metabolic pathways, including BCKDHA, acetyl-CoA carboxylase alpha (ACC1), ATP citrate lyase (ACL), nicotinamide adenine dinucleotide kinase (NADK), and tyrosine aminotransferase (TAT) (29), we investigated whether changes in BCKDK levels resulted in changes in levels of tissue metabolites in *Ube3b*<sup>−/−</sup> mice. We profiled the relative abundance of over 200 metabolites in plasma and cortical tissue from WT and *Ube3b*<sup>−/−</sup> mice. The metabolites represented pathways from amino acid biogenesis, the TCA cycle, glycolysis, the pentose phosphate pathway (PPP), and nucleotide metabolism, among others (Dataset S1). We detected 138 and 139 metabolites in plasma and cortex, respectively (Dataset S2 A and B), that clustered by genotype (Fig. 4A). Loss of UBE3B led to significant changes in levels of several metabolites in plasma and cortex (Fig. 4C and SI Appendix, Figs. S9 and S10). Metabolites that changed the most in *Ube3b*<sup>−/−</sup> plasma compared with WT were those belonging to the TCA cycle and nucleotide metabolism (SI Appendix, Fig. S9). In the cortex, significant changes were found in metabolites belonging to these two pathways as well as those from amino acid metabolism and glycolysis (SI Appendix, Fig. S10).

Given that several of the pathways implicated by the metabolomics survey occur in mitochondria and that UBE3B localizes to the mitochondria as well as the cytoplasm (30), we analyzed mitochondrial morphology in neural stem cells isolated from *Ube3b*<sup>−/−</sup> mice and control littermates. We found no changes in mitochondrial morphology (SI Appendix, Fig. S11). Thus, the changes observed using metabolomics did not appear to be due to a more generalized alteration in mitochondrial structure.

To examine the enzymatic activity of BCKDC, we measured branched-chain  $\alpha$ -ketoacid-induced mitochondrial respiration in brain, liver, and skeletal muscle of WT and *Ube3b*<sup>−/−</sup> mice. We found that mitochondria-enriched liver fractions from WT and *Ube3b*<sup>−/−</sup> mice showed no significant difference in respiratory activity in the presence of the BCKDC substrate  $\alpha$ -ketoisovaleric acid ( $\alpha$ -KIV), the  $\alpha$ -ketoacid of valine (Fig. 4E). No detectable BCKDC activity was observed in brain mitochondria (SI Appendix, Fig. S12). In contrast, we found that mitochondria-enriched fractions from skeletal muscle of *Ube3b*<sup>−/−</sup> mice had a ~2.55-fold reduction in  $\alpha$ -KIV-induced respiration (Fig. 4E).

These data suggest that BCKDK accumulation leads to reduced BCKDC activity only in skeletal muscle in *Ube3b*<sup>−/−</sup> mice. Consistent with this finding, phospho-BCKDHA was increased in skeletal muscle but not liver of *Ube3b*<sup>−/−</sup> mice (Fig. 4F). Taken together, the metabolic aberrations found in the tissues of *Ube3b*<sup>−/−</sup>

**Table 1. Proteomics identifies UBE3B interactors and candidate substrates**

Symbol	Name	NWD score	Z score
BCKDHA	Branched-chain $\alpha$ -ketoacid dehydrogenase E1, alpha polypeptide	0.77	8.91
BCKDK	Branched-chain $\alpha$ -ketoacid dehydrogenase kinase	1.03	9.38
CALM3	Calmodulin 3	2.13	9.63
CEP55	Centrosomal protein 55	1.54	10.42
CPNE7	Copine 7	2.18	11.00
DBT	Dihydrolipoamide branched-chain transacylase	3.39	11.49
DYNLRB2	Dynein light-chain roadblock-type 2	1.09	8.25
GTPBP8	GTP-binding protein 8	2.18	11.00
LAMC1	Laminin subunit gamma 1	3.09	11.71
LMNA	Lamin A/C	1.06	3.87
PAIP1	Poly(A) binding protein interacting protein 1	1.09	8.25
PPP3R1	Protein phosphatase 3 regulatory subunit B, alpha	2.18	11.00
PPP4R3C	Protein phosphatase 4 regulatory subunit 3C	2.18	11.00
PSMA1	Proteasome subunit alpha 1	1.78	10.98
PSMA3	Proteasome subunit alpha 3	1.22	10.98
PSMB1	Proteasome subunit beta 1	1.96	11.48
PSMB2	Proteasome subunit beta 2	1.89	9.55
PSMB3	Proteasome subunit beta 3	2.70	11.44
PSMB4	Proteasome subunit beta 4	3.06	11.57
PSMB7	Proteasome subunit beta 7	4.36	11.68
SF3A1	Splicing factor 3a subunit 1	1.04	0.55
UBE3B	Ubiquitin protein ligase E3B	21.49	11.66
ZBED4	Zinc finger BED-type containing 4	3.09	11.71

NWD, normalized weighted D-score.

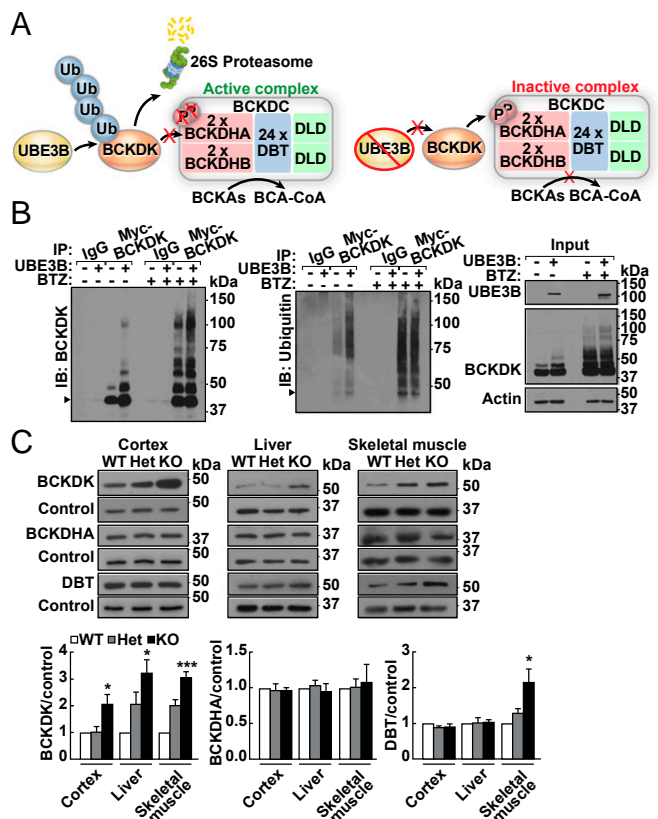


**Fig. 3.** UBE3B ubiquitinates BCKDK and targets it for degradation. (A) BCKDC catalyzes the oxidative decarboxylation of branched-chain  $\alpha$ -ketoacids (BCKAs), derivatives of BCAAs, into branched-chain acyl-CoA (BCA-CoA) species. UBE3B ubiquitinates BCKDK, targeting it for degradation. In the absence of UBE3B, BCKDK accumulates, resulting in increased phosphorylation of BCKDK and a decrease in complex activity. (B) UBE3B ubiquitinates BCKDK. HEK293T (–) or HEK293T stable cells expressing UBE3B-HA (+) were transfected with Myc-BCKDK and treated with bortezomib (BTZ) (+) or vehicle (–). Lysates were subject to denaturing immunoprecipitation (IP) with anti-Myc or IgG agarose, and IP fractions were analyzed by anti-Myc (Left) or anti-ubiquitin immunoblotting (IB) (Right). Arrowheads point to BCKDK (Left) and its 46-kDa band (Right). Higher molecular-weight bands correspond to ubiquitinated forms of BCKDK. Input fractions were analyzed by anti-Ube3b, anti-BCKDK, or anti-actin IB. (C, Top) Western blot of cortex, liver, or skeletal muscle of WT, Het, or KO mice shows accumulation of BCKDK but not BCKDHA in KO tissues. DBT accumulates in KO skeletal muscle but not in cortex or liver. (C, Bottom) Western blot quantifications. Values are mean  $\pm$  SEM (BCKDK: cortex  $*P = 0.0298$ , liver  $*P = 0.0162$ , skeletal muscle  $***P = 0.0003$ ; DBT:  $*P = 0.0235$ ; for each tissue  $n = 3$ –4 per genotype). Control refers to IB with anti-actin (cortex) or anti-GAPDH (glyceraldehyde-3-phosphate dehydrogenase; liver, skeletal muscle).

mice coupled with the identification of BCKDK as a UBE3B substrate suggest that KOS may be a metabolic encephalomyopathy with primary effects on multiple target organs.

**Altered Plasma Metabolomic Profile in Patients with KOS.** As part of our ongoing studies to understand the mechanisms underlying KOS, we identified two families where clinical whole-exome sequencing (WES) revealed pathogenic variants in *UBE3B*. The proband from the first family (UB-1) was a boy who was initially identified in infancy (UB-1–3). He had developmental delay, ID, lack of speech, microcephaly, hypotonia, and feeding difficulty (Table 2). WES revealed that he was a compound heterozygote for two missense mutations in *UBE3B*: p.Q642R (maternally inherited) and p.D963N (paternally inherited). The second family (UB-2) had two affected boys with KOS who were diagnosed at ages 3 and 6 (UB-2–3 and UB-2–4). The two brothers

had severe ID, lack of speech, microcephaly, hypoplastic corpus callosum, and feeding difficulty (Table 2). Both siblings were compound heterozygotes for mutations in *UBE3B*: a maternally inherited frameshift mutation and a paternally inherited splice acceptor mutation (Table 2). We validated the mutations using Sanger sequencing and determined segregation of the mutations in both families (Fig. 5 A and B).

Western blot of lysates from lymphoblastoid cell lines showed a complete loss of UBE3B in the two affected siblings from family UB-2 (UB-2–3 and UB-2–4) compared with unaffected controls (Fig. 5C). This suggests that these mutations result in nonsense-mediated mRNA decay. No change was seen in UBE3B level in the other proband (UB-1–3) compared with unaffected controls

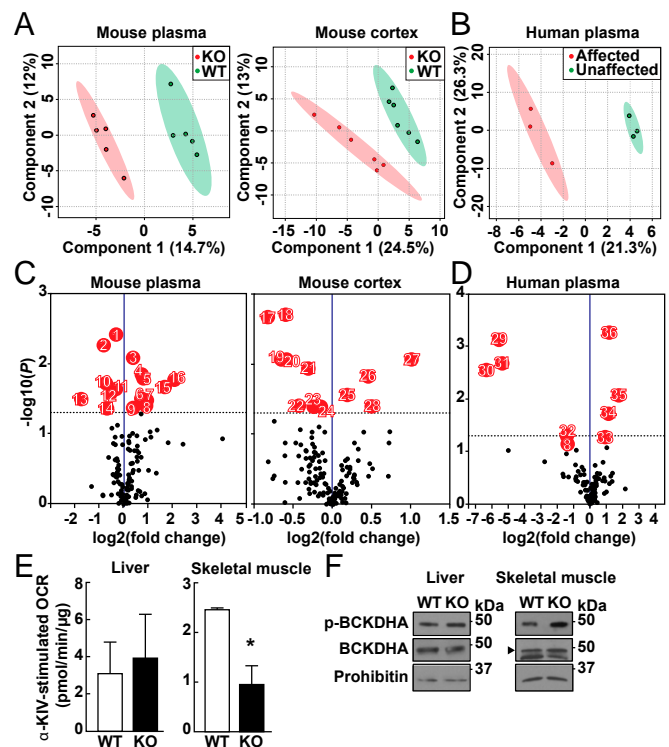


**Fig. 4.** Metabolic perturbations following loss of *Ube3b*. Metabolomics profiling from plasma and cortex of WT and KO mice ( $n = 5$ –6 WT, 5–6 KO) (A) and from plasma of KOS patients ( $n = 3$ : UB-1–3, UB-2–3, UB-2–4) and unaffected individuals ( $n = 3$ : UB-1–2, UB-2–1, UB-2–2) (B). Partial least squares discriminant analysis of metabolomics data. Metabolites altered in KO versus WT (C) and in affected versus unaffected individuals (D). Metabolites demonstrating significant changes in abundance are indicated in red, numbered, and individually plotted in *SI Appendix, Figs. S9, S10, and S13*. Dotted line represents  $P < 0.05$ . Mouse plasma (1: 4-hydroxybenzoic acid, 2: stearoylcarnitine, 3: pyridoxine, 4: uracil, 5: L-homoserine, 6: D-glutamic acid, 7: citric acid, 8: D-2-hydroxyglutaric acid, 9: thymidine, 10: tetradecanoylcarnitine, 11: choline, 12: 1-methyladenosine, 13: creatinine, 14: 1-methylnicotinamide, 15: S-adenosylhomocysteine, 16: spermidine), mouse cortex (17: niacinamide, 18: D-glucose, 19: L-lysine, 20: AICAR, 21: adenine, 22: propionylcarnitine, 23: cis-aconitic acid, 24: pipercolic acid, 25: shikimic acid, 26: 4-hydroxyproline, 27: phosphorylcholine, 28: urea), human plasma (29: guanine, 30: glucose-6-phosphate, 31: NAD, 32: adenosine, 33: creatine, 34: 5-aminolevulinic acid, 35: L-kynurenine, 36: 4-hydroxyproline). (E)  $\alpha$ -KIV-induced respiration measured from liver and skeletal muscle mitochondria shows a  $\sim 2.55$ -fold reduction in skeletal muscle from KO versus WT ( $*P = 0.0145$ ;  $n = 3$  WT, 3 KO). Values are mean  $\pm$  SEM. (F) Western blot of liver and skeletal muscle mitochondrial fractions shows increased phosphorylation of BCKDHA in skeletal muscle but not in liver from KO versus WT. Arrowhead points to BCKDHA band. Representative immunoblots from three independent experiments ( $n = 3$  WT, 3 KO).

**Table 2. Clinical phenotype of patients with *UBE3B* mutations**

Patient	UB-1-3	UB-2-3	UB-2-4
Sex	Male	Male	Male
Age, y	20	11	8
Nucleotide change	c.1925 A>G c.2887 G>A	c.256delC c.941-1 G>A	c.256delC c.941-1 G>A
Amino acid change	p.Gln642Arg p.Asp963Asn	p.Leu86TyrfsX19 IVS11-1 G>A	p.Leu86TyrfsX19 IVS11-1 G>A
MAF (percentage)	NP 0.0137	0.0016 NP	0.0016 NP
Weight (percentile)	< first	< fifth	third
Head circumference (percentile)	< 0.01	< fifth	< fifth
DD	+	+	+
ID	+	+	+
Absent speech	+	+	+
Seizures	-	-	+
Muscle hypotonia	+	+	+
Feeding difficulties	+	+	+
Facial dysmorphisms	+	+	+
Abnormal MRI	+	NR	NR

All findings reported at latest examination. Mutations are compound heterozygous and are reported on human genome GRCh37/hg19 coordinates and RefSeq transcript NM\_130466.3. DD, developmental delay; ID, intellectual disability; MAF, minor allele frequency in gnomAD; NP, not present; NR, not reported.

(Fig. 5C). It is possible that the missense mutations in UB-1-3 alter protein function or subcellular localization.

We profiled metabolite levels in plasma from the affected (UB-1-3, UB-2-3, UB-2-4) and unaffected (UB-1-2, UB-2-1, UB-2-2) individuals. We found that affected family members had differences in the abundance of 109 metabolites (Dataset S2C) that clustered by genotype (Fig. 4B). Several metabolites were significantly altered in plasma of affected individuals (Fig. 4D and SI Appendix, Fig. S13) and belonged to amino acid and nucleotide metabolism pathways, glycolysis and TCA cycle, energy metabolism, and heme biosynthesis (SI Appendix, Fig. S13).

## Discussion

In this study, we identified a role for *UBE3B* in neuronal development and behavior, discovered an *in vivo* substrate for *UBE3B*, and gained insight into the disease mechanism in KOS. *Ube3b*<sup>-/-</sup> mice recapitulate phenotypes of KOS patients—namely, reduced growth, brain size, and muscle strength; lack of vocalization; and hypoplastic corpus callosum. *Ube3b*<sup>-/-</sup> mice also have enlarged ventricles and decreased thickness of the somatosensory cortex. We found that *Ube3b* is expressed in the hippocampal pyramidal layer and cortical layers II/III and V, among other brain regions, and identified a role for *UBE3B* in dendritic morphogenesis. In addition, *Ube3b*<sup>-/-</sup> cortical neurons showed a reduction in the presynaptic marker synapsin I and an increase in the postsynaptic marker PSD95, suggesting that these neurons are less mature and that loss of *Ube3b* may affect vesicle organization at synaptic terminals. *Ube3b*<sup>-/-</sup> cortical neurons had abnormalities in the number of VGAT-positive inhibitory synaptic puncta, suggesting delayed maturation of inhibitory neurons.

We identified several *UBE3B* interactors, including calmodulin-regulated protein phosphatase PPP3R1 (the calcium-binding subunit of calcineurin), a calmodulin, a calcium-dependent lipid-binding protein, a centrosomal protein that regulates cytokinesis, multiple proteasome subunits, and three members of the BCAA metabolism pathway (BCKDK, BCKDHA, and DBT). We found that *UBE3B* ubiquitinates BCKDK and targets it for degradation by the proteasome. BCKDK was initially identified as the kinase that phosphorylates BCKDHA, thus inactivating BCKDC. However, a recent study identified additional phosphorylation targets of BCKDK, including enzymes that function in lipogenesis (ACL), tyrosine

transamination (TAT), and phosphorylation of nicotinamide adenine dinucleotide (NAD; NADK) (29). NADK phosphorylation of NAD generates NADP, which in turn enters the PPP to generate NADPH (the reduced form of NADP) and precursors for nucleotide biosynthesis. ATP-citrate lyase (ACL) is a key enzyme in lipogenesis, a process critical for neuronal differentiation (31). BCKDK accumulation may disrupt the regulation of lipogenesis in developing neurons of *Ube3b*<sup>-/-</sup> mice. Complete loss-of-function mutations in *BCKDK* result in ID, ASD, and epilepsy (27). Importantly, duplications spanning the *BCKDK* locus, including those at chromosome 16p11.2, result in a spectrum of neurodevelopmental phenotypes comprising developmental delay, speech and language abnormalities, ID, ASD, and microcephaly (13, 32, 33). Thus, human genetics data, combined with our data from *Ube3b*<sup>-/-</sup> mice, suggest that BCKDK plays an important role in brain development and function, and that overexpression of *BCKDK* may underlie the neurodevelopmental phenotypes observed in patients with duplications spanning the locus.

Additionally, we report on the first posttranslational modification of BCKDK as a mechanism to regulate its levels. Loss of *Ube3b* resulted in BCKDK accumulation in cortex, liver, and skeletal muscle of *Ube3b*<sup>-/-</sup> mice. Metabolomics profiling revealed that this accumulation led to changes in the levels of several metabolites from nucleotide and amino acid metabolism pathways, glycolysis, and TCA cycle. Metabolomics profiling in plasma from KOS patients revealed similar metabolic changes. In *Ube3b*<sup>-/-</sup> plasma, levels of several TCA-cycle metabolites were increased (citric acid, 2-hydroxyglutaric acid, glutamic acid, and succinic acid), suggesting that the TCA cycle is disrupted. Levels of choline, a precursor of acetylcholine, were decreased in *Ube3b*<sup>-/-</sup> plasma, while phosphorylcholine levels were increased in *Ube3b*<sup>-/-</sup> cortex. In *Ube3b*<sup>-/-</sup> cortex, there was a decrease in levels of adenine, 5-aminoimidazole-4-carboxamide ribonucleotide (AICAR), and niacinamide, all part of nucleotide metabolism pathways. Purine metabolites were also reduced in plasma from KOS patients—specifically, guanine, adenosine, and NAD—the last of which also functions in a multitude of pathways. In addition, glucose 6-phosphate was significantly reduced in plasma from KOS patients. Inborn errors of purine metabolism represent

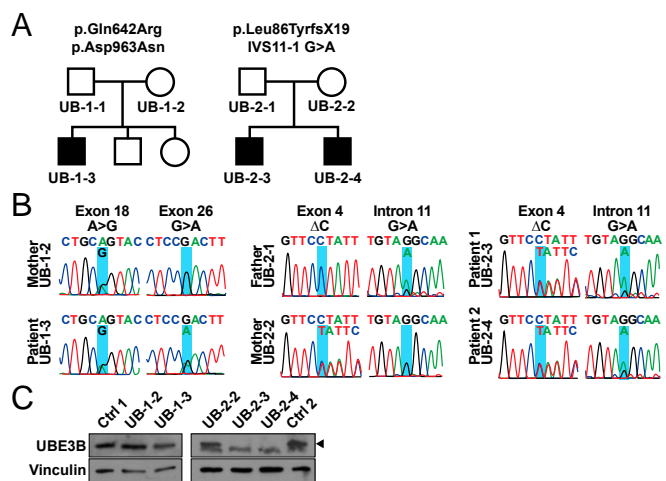


**Fig. 5.** Identification of recessive *UBE3B* mutations in two families with KOS. (A) Pedigrees of two families with compound heterozygous *UBE3B* mutations in three children affected by KOS. Shaded symbols indicate affected individuals. (B) Sanger-sequencing results for individuals from UB-1 and UB-2 confirmed segregation of *UBE3B* variants detected by clinical WES. (C) Western blot of lymphoblastoid cell line lysates from affected individuals (UB-1-3, UB-2-3, UB-2-4), unaffected family members (UB-1-2, UB-2-2), and two unrelated controls (Ctrl 1, Ctrl 2) show loss of *UBE3B* in affected individuals (UB-2-3 and UB-2-4). Vinculin is a loading control. Arrowhead points to *UBE3B* band.

a rare class of disorders that result in a spectrum of clinical presentations, including severe neurological phenotypes (34).

Despite increased BCKDK in cortex, liver, and skeletal muscle from *Ube3b*<sup>-/-</sup> mice, we did not observe any significant changes in BCAAs or their metabolites in plasma and cortex from *Ube3b*<sup>-/-</sup> mice or in plasma from KOS patients (*SI Appendix, Fig. S14*). One explanation is that BCAA metabolites feed into other pathways (for example, the TCA cycle) and, since BCKDK regulates some of these pathways, there is a less pronounced effect on BCAA metabolism when BCKDK levels are elevated. On the other hand, in disorders where BCKDC subunits are defective (e.g., MSUD) or where BCKDK is deficient, there is a more direct effect on BCAA metabolism. However, when BCKDK levels are high, there is a significant effect on the TCA cycle and nucleotide metabolism. Another possibility is that the effect of BCKDK on BCAA metabolism is counteracted in brain and liver but not skeletal muscle of *Ube3b*<sup>-/-</sup> mice by the activity of PPM1K, the phosphatase that activates BCKDC.

Our findings that BCKDC activity is decreased specifically in skeletal muscle and that *Ube3b*<sup>-/-</sup> mice have reduced grip strength suggest that KOS is a multiorgan disease that includes a primary muscle deficit, classifying it as a metabolic encephalomyopathy. Furthermore, for the following reasons our data suggest that KOS is not a phenocopy of MSUD. In KOS, a partial defect in BCKDC activity is expected since BCKDC subunits are intact; thus, the consequences for BCAA metabolites are blunted in KOS. The decreased BCKDC activity

observed in skeletal muscle of *Ube3b*<sup>-/-</sup> mice may be responsible for the observed myopathy, while the normal activity in liver prevents the metabolic changes seen in MSUD. Finally, the increase in BCKDK levels in KOS results in perturbations in multiple metabolic pathways. Collectively, this indicates that KOS and MSUD are not phenocopies and, as a consequence, the standard therapies implemented in patients with MSUD, such as diet modification and liver transplantation, may not work for patients with KOS. Treatment strategies designed to target BCKDK may have beneficial clinical effects in KOS.

## Materials and Methods

The study was approved by the University of Texas Southwestern Medical Center (UTSW) Institutional Review Board, and written informed consent was obtained from participants. Phenotypes of affected individuals along with a detailed description of all materials and methods for generation of *Ube3b*<sup>-/-</sup> mice, analysis of neurobehavioral phenotypes, proteomics, and metabolomics are detailed in the *SI Appendix, SI Materials and Methods*.

**ACKNOWLEDGMENTS.** We are grateful to the families for their invaluable participation in our study. We thank Dr. R. Hammer and the UTSW Transgenic Core facility; Drs. J. W. Harper and L. Pontano-Vaites for mass spectrometry; Dr. R. DeBerardinis and L. Zacharias for metabolomics profiling; Dr. E. Plautz in the UTSW Neuro-Models Core Facility for the grip strength test; C. Burroughs for assistance with figures; and Dr. G. Konopka for her helpful comments on the manuscript. M.H.C. was supported by UTSW, a NARSAD Young Investigator grant from the Brain and Behavior Research Foundation, and a National Institute of Mental Health Grant (R21 MH115313).

- Centers for Disease Control and Prevention (CDC) (2004) Economic costs associated with mental retardation, cerebral palsy, hearing loss, and vision impairment—United States, 2003. *MMWR Morb Mortal Wkly Rep* 53:57–59.
- Boyle CA, et al. (2011) Trends in the prevalence of developmental disabilities in US children, 1997–2008. *Pediatrics* 127:1034–1042.
- Developmental Disabilities Monitoring Network Surveillance Year 2010 Principal Investigators; Centers for Disease Control and Prevention (CDC) (2014) Prevalence of autism spectrum disorder among children aged 8 years—Autism and developmental disabilities monitoring network, 11 sites, United States, 2010. *MMWR Surveill Summ* 63:1–21.
- Leigh JP, Du J (2015) Brief report: Forecasting the economic burden of autism in 2015 and 2025 in the United States. *J Autism Dev Disord* 45:4135–4139.
- Le Hellard S, Steen VM (2014) Genetic architecture of cognitive traits. *Scand J Psychol* 55:255–262.
- Colvert E, et al. (2015) Heritability of autism spectrum disorder in a UK population-based twin sample. *JAMA Psychiatry* 72:415–423.
- Plomin R, DeFries JC, Knopik VS, Neiderhiser J (2013) *Behavioral Genetics* (Worth Publishers, New York), 6th Ed.
- Betancur C (2011) Etiological heterogeneity in autism spectrum disorders: More than 100 genetic and genomic disorders and still counting. *Brain Res* 1380:42–77.
- Neale BM, et al. (2012) Patterns and rates of exonic de novo mutations in autism spectrum disorders. *Nature* 485:242–245.
- Sanders SJ, et al. (2012) De novo mutations revealed by whole-exome sequencing are strongly associated with autism. *Nature* 485:237–241.
- De Rubeis S, et al.; DDD Study; Homozygosity Mapping Collaborative for Autism; UK10K Consortium (2014) Synaptic, transcriptional and chromatin genes disrupted in autism. *Nature* 515:209–215.
- OMIM (Online Mendelian Inheritance in Man); McKusick-Nathans Institute of Genetic Medicine; Johns Hopkins University, Baltimore.
- The DDD Study (2015) Large-scale discovery of novel genetic causes of developmental disorders. *Nature* 519:223–228.
- Basel-Vanagaite L, et al. (2012) Deficiency for the ubiquitin ligase UBE3B in a blepharophimosis-ptosis-intellectual-disability syndrome. *Am J Hum Genet* 91:998–1010.
- Basel-Vanagaite L, et al. (2014) Expanding the clinical and mutational spectrum of Kaufman oculocerebrofacial syndrome with biallelic UBE3B mutations. *Hum Genet* 133:939–949.
- Flex E, et al. (2013) Loss of function of the E3 ubiquitin-protein ligase UBE3B causes Kaufman oculocerebrofacial syndrome. *J Med Genet* 50:493–499.
- Karimnejad A, et al. (2017) Kaufman oculo-cerebro-facial syndrome in a child with small and absent terminal phalanges and absent nails. *J Hum Genet* 62:465–471.
- Pedurupillay CR, et al. (2015) Kaufman oculocerebrofacial syndrome in sisters with novel compound heterozygous mutation in UBE3B. *Am J Med Genet A* 167A:657–663.
- Yilmaz R, et al. (2018) Kaufman oculocerebrofacial syndrome: Novel UBE3B mutations and clinical features in four unrelated patients. *Am J Med Genet A* 176:187–193.
- Chahrour MH, et al.; ARRA Autism Sequencing Collaboration (2012) Whole-exome sequencing and homozygosity analysis implicate depolarization-regulated neuronal genes in autism. *PLoS Genet* 8:e1002635.
- Kishino T, Lalonde M, Wagstaff J (1997) UBE3A/E6-AP mutations cause Angelman syndrome. *Nat Genet* 15:70–73.
- Froyen G, et al. (2008) Submicroscopic duplications of the hydroxysteroid dehydrogenase HSD17B10 and the E3 ubiquitin ligase HUWE1 are associated with mental retardation. *Am J Hum Genet* 82:432–443.
- Küry S, et al. (2017) De novo disruption of the proteasome regulatory subunit PSMD12 causes a syndromic neurodevelopmental disorder. *Am J Hum Genet* 100:352–363.
- O’Roak BJ, et al. (2012) Sporadic autism exomes reveal a highly interconnected protein network of de novo mutations. *Nature* 485:246–250.
- Sowa ME, Bennett EJ, Gygi SP, Harper JW (2009) Defining the human deubiquitinating enzyme interaction landscape. *Cell* 138:389–403.
- Brosnan JT, Brosnan ME (2006) Branched-chain amino acids: Enzyme and substrate regulation. *J Nutr* 136(Suppl 1):2075–2115.
- Novarino G, et al. (2012) Mutations in BCKDK-kinase lead to a potentially treatable form of autism with epilepsy. *Science* 338:394–397.
- Herring WJ, Litwer S, Weber JL, Danner DJ (1991) Molecular genetic basis of maple syrup urine disease in a family with two defective alleles for branched chain acyltransferase and localization of the gene to human chromosome 1. *Am J Hum Genet* 48:342–350.
- White PJ, et al. (2018) The BCKDH kinase and phosphatase integrate BCAA and lipid metabolism via regulation of ATP-citrate lyase. *Cell Metab* 27:1281–1293.e7.
- Braganza A, et al. (2017) UBE3B is a calmodulin-regulated, mitochondrion-associated E3 ubiquitin ligase. *J Biol Chem* 292:2470–2484.
- Ziegler AB, et al. (2017) Cell-autonomous control of neuronal dendrite expansion via the fatty acid synthesis regulator SREBP. *Cell Rep* 21:3346–3353.
- Bernier R, et al.; Simons VIP consortium (2017) Developmental trajectories for young children with 16p11.2 copy number variation. *Am J Med Genet B Neuropsychiatr Genet* 174:367–380.
- Steinman KJ, et al.; Simons VIP Consortium (2016) 16p11.2 deletion and duplication: Characterizing neurologic phenotypes in a large clinically ascertained cohort. *Am J Med Genet A* 170:2943–2955.
- Balasubramaniam S, Duley JA, Christodoulou J (2014) Inborn errors of purine metabolism: Clinical update and therapies. *J Inher Metab Dis* 37:669–686.

## Supplementary Information for

The ubiquitin ligase UBE3B, disrupted in intellectual disability and absent speech, regulates metabolic pathways by targeting BCKDK

Solmi Cheon, Kiran Kaur, Nadine Nijem, Islam Oguz Tuncay, Pooja Kumar, Milan Dean, Jane Juusola, Maria J. Guillen-Sacoto, Emma Bedoukian, Lynne Ierardi-Curto, Paige Kaplan, G. Bradley Schaefer, Prashant Mishra, Maria H. Chahrour

Maria H. Chahrour

Email: [maria.chahrour@utsouthwestern.edu](mailto:maria.chahrour@utsouthwestern.edu)

### **This PDF file includes:**

Supplementary text  
Figs. S1 to S14  
Captions for Datasets S1 and S2  
References for SI reference citations

### **Other supplementary materials for this manuscript include the following:**

Datasets S1 and S2

## Supplementary Information Text

### SI Materials and Methods

#### Subjects and specimens

The study was approved by the University of Texas Southwestern Medical Center (UTSW) Institutional Review Board. Two families, UB-1 and UB-2, with KOS and *UBE3B* mutations (Table 2) were identified through GeneDx and enrolled in our study after obtaining written informed consent from all study participants. Subjects were evaluated in a clinical setting and phenotypes of the affected individuals are detailed below. Peripheral blood samples were collected from the affected individuals and family members. Genomic DNA was isolated from circulating leukocytes using AutoPure (Qiagen) according to the manufacturer's instructions. Targeted Sanger sequencing was used to confirm variants that were identified by clinical whole exome sequencing (GeneDx). Lymphocytes were isolated and Epstein-Barr virus-transformed lymphoblastoid cell lines were generated at the UTSW Human Genetics Clinical Laboratory.

#### Clinical presentation

##### *Family UB-1*

The first proband (UB-1-3) is a boy from a United States family of European ancestry. The proband has two unaffected siblings, a male and a female. The proband presented before the age of 1 with significant developmental delay, poor growth, microcephaly, and muscle hypotonia, with weight, length, and head circumference below the 3<sup>rd</sup> percentile. The patient did not sit without support until 14 months of age and started crawling at 16 months of age. He had lactic acidosis (plasma lactate of 3.2 mmol/L, normal range: 0.6-2.0 mmol/L) at presentation, that spontaneously resolved. By 7 years of age he had poor fine and gross motor skills. He could walk unsteadily with support, but gradually lost this ability. He had developed a modified pincer grasp, which was gradually lost. In childhood, he could respond to questions with guttural sounds, and by adolescence, he had complete lack of speech. His hearing was normal. He had optic nerve atrophy and congenital cataracts. His muscle hypotonia developed into hypertonia and spastic diplegia. He had facial dysmorphisms (deep set eyes with narrow palpebral fissures, full lips, and large teeth) and short trident fingers with mild cutaneous syndactyly and convex nails. Other findings included intermittent thrombocytopenia, severe obstructive sleep apnea treated with continuous positive airway pressure (CPAP), and frequent pneumonia infections with presumed chronic lung disease secondary to aspiration. On physical exam at age 18 his head circumference was 47 cm (<0.01 percentile, z-score -4.26; average for 1 year of age), his height was 111.2 cm (<1<sup>st</sup> percentile; average for 5 years of age), and his weight was 33.8 kg (<1<sup>st</sup> percentile; average for 4 years of age). He was unable to eat by mouth and required feeding via a gastrostomy (g)-tube. He developed hypertension with thick left ventricle, diabetes mellitus type 2, proteinuria, and renal insufficiency. Secondary adrenal insufficiency manifested at age 20.

His first imaging study was performed at 13 months of age. Brain magnetic resonance imaging (MRI) found prolonged T1 and T2 relaxation rates in superior pons, midbrain, hypothalamus, and left basal ganglia

that were increasing when repeat scanning was done two months later. At 15 months of age, MRI showed cerebral volume loss, delay in myelination, and abnormal signal involving the cerebral peduncles and dorsal brainstem. MR spectroscopy at 2 years of age demonstrated elevated lactate levels in the basal ganglia. A subsequent MRI at 8 years of age showed marked global cerebral and cerebellar volume loss, and signal alteration within the bilateral basal ganglia and periventricular white matter.

### **Family UB-2**

The second set of probands are siblings from an African American family from the United States. UB-2-3 presented at the age of 6 with severe ID, lack of speech (he had only 2-3 words), microcephaly, mild to moderate sensorineural hearing loss (SNHL), optic nerve anomaly, facial dysmorphisms (ptosis, retrognathism, small low set ears, and preauricular tags), pes cavus, and hammer toes. On brain imaging he was found to have hypoplasia of the corpus callosum. His development was significantly delayed, walking at 3 years of age. At 11 years of age his head circumference was 51.6 cm (<5<sup>th</sup> percentile), his height was 141.8 cm (20<sup>th</sup> percentile), and his weight was 27.4 kg (<5<sup>th</sup> percentile). Other findings included thoracolumbar scoliosis, bilateral hallux valgus, right inguinal hernia, umbilical hernia, peripheral neuropathy, and sleep disorder. He was also noted to have oppositional defiant disorder.

His brother (UB-2-4) presented with similar clinical features at the age of 3. He was born full term but spent 8 months in the neonatal intensive care unit for poor growth. Although he was born weighing 3.2 kg, at 8 years of age he weighed 20.2 kg (3<sup>rd</sup> percentile), had a height of 125.1 cm (35<sup>th</sup> percentile), and a head circumference of 51.2 cm (<5<sup>th</sup> percentile). He presented with severe ID, facial dysmorphisms (ptosis, retrognathism, malocclusion, and small low set ears), and dysphagia (requiring a g-tube). Additional findings included SNHL, optic nerve anomaly, myopia, astigmatism, peripheral neuropathy, scoliosis, pes cavus, and hammer toes. He was also found to have mild obstructive sleep apnea. His overall development was delayed, sitting unsupported at 12 months of age, crawling at 24 months of age, and walking at 3 years of age. He had a single episode of seizure at 8 years of age. MRI identified asymmetry of the transverse-sigmoid sinus.

### **Patient lymphoblastoid cell lines**

Cells were cultured in RPMI-1640 with 2 mM L-Glutamine, 10% fetal bovine serum (FBS), 1% v/v penicillin-streptomycin solution, and 1% v/v Fungizone. For immunoblotting, cells were lysed in SDS lysis buffer and western blot analysis was performed as described above. Primary antibodies used were: Ube3b (Synaptic Systems, 339003, 1:500) and Vinculin (Cell Signaling, 4650S, 1:1,000).

### **Generation of *Ube3b* constitutive knockout mice**

*Ube3b* tm1a targeted embryonic stem (ES) cells (ES cell line JM8.F6; strain C57BL/6N) were obtained from the European Mammalian Mutant Cell Repository (EUCOMM). The ES cells are heterozygous for a targeted trap allele of *Ube3b*, generated by targeting the endogenous *Ube3b* locus between exons 6 and 8 with a promoterless selection cassette containing the LacZ gene (flanked by *Frt* sequences) and neomycin for positive selection of targeted ES cell clones. Exon 7 of *Ube3b* was flanked by loxP sequences (Fig. S1A). The

targeted ES cell clones were injected into albino C57BL/6-*Tyr<sup>c-Brd</sup>* blastocysts to generate chimeras at the Transgenic Core of UTSW. Resultant male chimeras were bred to wild type (WT) albino females C57BL/6BrdCrHsd-*Tyr<sup>c</sup>* (Envigo) to transmit the targeted allele. Heterozygous targeted mice were intercrossed to confirm germline transmission, and F2 progeny were backcrossed to C57BL/6N for 2 generations and maintained on a C57BL/6N background. Mice were genotyped by PCR with three primers as follows: forward (WT), 5'-AACCAGGGAAACCGTCC-3' (binds only if there is no loxP sequence); forward (Flx), 5'-TCGTATAGCATACATTATACGAAGTT-3' (binds to loxP sequence); reverse (binds to both WT and Flx alleles), 5'-CGGAGACTACGGGCTACAAC-3'. Homozygous WT DNA produced a 242-bp band in the WT reaction and no band in the Flx reaction, while homozygous targeted DNA produced a 258-bp band in the Flx reaction and no band in the WT reaction (Fig. S1B). We confirmed loss of *Ube3b* mRNA and protein using quantitative RT-PCR and western blotting, respectively (Figs. S1B and S1C). The resulting constitutive *Ube3b<sup>+/-</sup>* mice were bred as *Ube3b<sup>+/-</sup>* x *Ube3b<sup>+/-</sup>* for all experiments. All animal care and use was approved by the UTSW Institutional Animal Care and Use Committee and is compliant with US Government principles about the care and use of animals, Public Health Service Policy on Humane Care and Use of Laboratory Animals, Guide for the Care and Use of Laboratory Animals, and the Animal Welfare Act. Animal husbandry was performed in the UTSW animal facility, accredited by the Association for Assessment and Accreditation of Laboratory Animal Care International.

### **Primary neuronal cultures**

Embryonic day (E) 18.5 embryos were collected from pregnant *Ube3b<sup>+/-</sup>* female mice that were mated to *Ube3b<sup>+/-</sup>* male mice. Cortices were dissected under a light microscope and dissociated with papain (Worthington Biochemical). Cells were resuspended in plating medium (Neurobasal, 10% FBS, 2% B27, 1% N2, 0.5 mM L-Glutamine, 25  $\mu$ M Glutamate, 1% v/v penicillin-streptomycin) and seeded at a density of 20 X 10<sup>4</sup> cells per well in a 24-well plate on a laminin/poly-L-ornithine coated glass coverslip. The next day, existing media was replaced with feeding media (2% B27, 1% N2, 0.5 mM L-Glutamine, 1% v/v penicillin-streptomycin). Cells were treated with 2  $\mu$ M Cytosine  $\beta$ -D-arabinofuranoside hydrochloride (Sigma, C6645) by replacing half of the existing media after 2 days in vitro (DIV). Subsequently, half of the media was replaced by fresh media every 3-4 days. At DIV5, cells were sparsely transfected with a GFP expressing plasmid (pCAG-EGFP) using Lipofectamine 2000 (Invitrogen). For transfection, the existing ("conditioned") media was replaced with serum- and antibiotics-free media, cells were incubated with DNA-Lipofectamine complexes (500 ng of plasmid DNA per well) for 2 hr, and subsequently recovered in the conditioned media. At DIV7, cells were fixed with 4% paraformaldehyde (PFA) for immunocytochemistry.

### **Quantitative RT-PCR**

For RT-PCR, RNA was isolated using Trizol reagent (Invitrogen) and RNeasy Mini Kit (Qiagen). DNA was removed using RNase-free DNase kit (Qiagen) and 0.25-2  $\mu$ g of RNA was used to synthesize cDNA with the Superscript III First Strand Synthesis System for RT-PCR (Invitrogen). Quantitative PCR was carried out using PowerUp SYBR Green (2X) master mix (Applied Biosystems) and the following primers:

*Ube3b* forward: 5'-AGAGATCTTACAGGACTCCAGG-3', and reverse: 5'-GATGGCCCATTATATTTGCGC-3'

*Bckdk* forward: 5'-GACCTATGCATGGCTTTGGC-3', and reverse: 5'-CCGTAGGTAGACATCCGTGC-3'

*Bckdha* forward: 5'-TGGCTAGATCTCACCCCAGC-3', and reverse: 5'-ATGCCGGAGATGACATTGGG-3'

*Dbt* forward: 5'-TCAGACTGACCTGTGTTTCGC-3', and reverse: 5'-GTTCTCAGGGAGTGACGTGG-3'

*Gapdh* forward: 5'-CAAGGAGTAAGAAACCCTGGACC-3', and reverse: 5'-CGAGTTGGGATAGGGCCTCT-3'

### **Immunoprecipitation and mass spectrometry**

A human *UBE3B* cDNA clone was obtained from GeneCopoeia (Y3553, NM\_130466.3) and cloned into pDONR223. The clone was sequence validated and recombined into the Gateway destination vector pHAGE-C-FLAG-HA via  $\lambda$  recombination following the Gateway protocol (Invitrogen), to generate a C-terminally tagged UBE3B-HA construct in a lentiviral expression vector. Lentivirus carrying the C-terminally tagged UBE3B-HA was produced by co-transfecting with lentiviral helper plasmids into HEK293T cells and used to infect HEK293T which subsequently underwent selection with 1  $\mu$ g/ml puromycin, to generate a stable cell line expressing UBE3B-HA, HEK293T<sup>UBE3B-HA</sup>. Protein expression was confirmed by immunoprecipitation and western blot (Fig. S7A). Cells were collected in cold 1X PBS and cell pellets were lysed in mammalian cell lysis buffer (50 mM Tris pH 7.5, 150 mM NaCl, 0.5% NP40) containing 2 mM OPT (1,10-Phenanthroline monohydrate), and cOmplete mini EDTA-free protease inhibitor and phosSTOP phosphatase inhibitor tablets (Roche). Lysates were incubated with monoclonal anti-HA-conjugated agarose beads (Sigma, A2095) at 4°C overnight. The beads were washed several times in lysis buffer, and the bound immunocomplexes were eluted with HA peptide. Following TCA precipitation and trypsin digestion, peptides were purified using StageTips (1) and subjected to LC-MS/MS using an LTQ linear ion trap mass spectrometer (Thermo Fisher). Methods, including data analysis, were carried out as previously described (2). For coimmunoprecipitation experiments to validate the MS data (Fig. S7B), cells were lysed and complexes were immunoprecipitated as described above, except agarose beads were boiled for western blot analysis.

### **Denaturing immunoprecipitation**

To immunoprecipitate BCKDK, Myc-Bckdk and His-Ub were transfected into the HEK293T cell line stably expressing UBE3B-HA. For BCKDHA and DBT immunoprecipitation, only His-Ub was transfected. Thirty-six hours (hr) post transfection, the cells were treated with DMSO or 50 nM Bortezomib (Thermo Fisher Scientific, 50-741-9) and harvested 16 hr post treatment. Cell pellets were lysed in modified mammalian lysis buffer (50 mM Tris pH 7.5, 150 mM NaCl, 0.5% Igepal CA-630, 1mM EDTA) containing 1 mM NaF, 1 mM Na<sub>3</sub>VO<sub>4</sub>, 2 mM OPT, 1 mM phenylmethylsulfonyl fluoride, 10 mM N-Ethylmaleimide (NEM), cOmplete mini EDTA-free protease inhibitor and phosSTOP phosphatase inhibitor tablets and boiled for 10 min after adding 0.1 volume (v) of 10% SDS. The lysates were diluted by adding 1 v of 10% Triton X-100 and 8 v of the lysis buffer and cleared by centrifugation. The supernatants were incubated at 4°C overnight with rabbit anti-c-Myc Agarose Affinity Gel (Sigma, A7470) to immunoprecipitate BCKDK and either anti-BCKDHA (Sigma, SAB2702057) or anti-DBT (Abcam, ab151991) with recombinant Protein G agarose (Novex) to immunoprecipitate endogenous

BCKDHA or DBT, respectively. The beads were washed with the lysis buffer three times and boiled with 1X SDS sample buffer. The eluates were used for western blot analysis.

### **Western blot and antibodies**

To detect endogenous proteins, cortical, liver, or skeletal muscle tissue was isolated from male and female mice and immediately frozen in liquid nitrogen. Cortical and liver tissue were lysed in SDS lysis buffer (250 mM Tris pH 6.8, 4% SDS, 3.2% glycerol, 10 mM NEM, 1 mM PMSF) supplemented with 2 mM OPT, and cComplete mini EDTA-free protease inhibitor and phosSTOP phosphatase inhibitor tablets (Roche). Frozen skeletal muscle was pulverized followed by lysis in the same SDS buffer used for cortical and liver tissue. Individual samples were sonicated, boiled, and centrifuged at 18,800 x *g* for 10 minutes (min). For analysis of mitochondrial proteins, mitochondria were isolated from liver, brain, and skeletal muscle as described below under "Enzymatic activity assays". Samples were diluted in 2X sample buffer (0.25 M Tris-HCl, pH 6.8; 4% SDS; 6.4% glycerol) containing  $\beta$ -mercaptoethanol and boiled for 5 min. Protein concentrations were determined using the bicinchoninic acid (BCA) protein assay (Sigma). Samples were diluted with sample buffer and 5-40  $\mu$ g of protein was loaded per lane onto either 6% (for Ube3b) or 8% polyacrylamide gels. Gels were run and protein was transferred to polyvinylidene difluoride (PVDF) membranes (Millipore) for 2 hr on ice. Membranes were blocked in 5% milk in TBS-T (20 mM Tris pH 7.5, 150 mM NaCl, 0.1% Tween-20) for 1 hr at room temperature, and incubated with primary antibody overnight at 4°C (for Ube3b, BCKDK, BCKDHA, phospho-BCKDHA, prohibitin, Myc, and ubiquitin) or for 2 hr at room temperature (for DBT,  $\beta$ -actin, and GAPDH). Membranes were washed in 5% TBS-T followed by a 1 hr incubation in secondary antibody (1:5,000 or 1:10,000 dilution) at room temperature using donkey anti-rabbit (Jackson ImmunoResearch, 711-035-152) or peroxidase AffiniPure donkey anti-mouse (Jackson ImmunoResearch, 715-035-150). Following antibody incubation, signal was detected with enhanced chemiluminescence (ECL; SuperSignal West Pico chemiluminescent substrate, Thermo Fisher Scientific). For coimmunoprecipitation experiments (Fig. S7B), fluorophore-conjugated secondary antibodies were used (LI-COR Biosciences) and signal was detected on an Odyssey Imager (LI-COR Biosciences). Bands were quantified using ImageJ (3), normalized to the appropriate loading control ( $\beta$ -actin or GAPDH), and analyzed using GraphPad Prism. Primary antibodies used were: Ube3b (Synaptic Systems, 339003, 1:500), BCKDK (Abcam, ab151297, 1:1,000), BCKDHA (Sigma, SAB2702057, 1:1,000), phospho-BCKDHA (Abcam, ab200577, 1:1,000), DBT (Abcam, ab151991, 1:5,000), ubiquitin (Cell Signaling, 3936S, 1:1,000), Myc (Abcam, ab18185, 1:1,000), HA (Abcam, ab9110, 1:10,000),  $\beta$ -actin (Abcam, ab6276, 1:10,000), GAPDH (Cell Signaling, 5174S, 1:10,000),  $\alpha$ -tubulin (Abcam, ab18251, 1:5,000), and prohibitin (Abcam, ab28172, 1:1,000).

### **Immunofluorescence and confocal microscopy**

Neurons were fixed in 4% PFA. Following fixation, neurons were incubated in blocking buffer (5% goat serum and 0.1% Triton X-100 in PBS). Primary and secondary antibodies were diluted in blocking buffer. The neurons were incubated overnight at 4°C with anti-GFP (Abcam, ab13970, 1:500) and different combinations of anti-

PSD95 (Thermo Fisher Scientific, MA1-045 or 51-6900, 1:500), anti-Synapsin I (Synaptic Systems, 106001, 1:500), and anti-VGAT (Synaptic Systems, 131002, 1:500). Neurons were incubated for 1 hr at room temperature in 1:1,000 dilutions of the following secondary antibodies: Alexa Fluor 488, Alexa Fluor 555, and Alexa Fluor 647 (Invitrogen). DAPI (Thermo Fisher Scientific, 62248) was used to stain nuclei. Coverslips were mounted with ProLong Gold Antifade Mountant (Invitrogen). GFP-positive neurons were imaged on a Zeiss LSM880 with 63X objective at 250 nm steps (10 steps) in z axis.

### **Sholl and synapse analyses**

Images were processed and analyzed in Fiji (4) using the “Sholl” plugin, and synapses were quantified using the macro “Synapse-Count-macro-for-Fiji” (5).

### **Golgi-Cox staining**

Mice were anesthetized with a ketamine/xylazine cocktail and brains were removed. Golgi-Cox staining was performed as described in Zaqout et al. 2016 (6). The brains were impregnated with Golgi-Cox solution (1%  $K_2Cr_2O_7$ , 1%  $HgCl_2$ , 0.8%  $K_2CrO_4$ ) at room temperature for 8 days in the dark. Subsequently, they were protected with tissue protectant solution (30% sucrose, 1% PVP40, 30% ethylene glycol in 0.05 M phosphate buffer pH 7.2) at 4°C for 7 days. The solution was replaced with a fresh one every 24 hr. Brains were cut into two hemispheres and embedded in OCT medium. Frozen sagittal sections (150  $\mu m$  thickness) were prepared using a microtome (Leica) and loaded on 3% gelatin-coated glass slides. The slides were dried for 3 days at room temperature, dehydrated, and developed as described in Zaqout et al. 2016 (6), and mounted with Cytoseal (Thermo Fisher Scientific). Brightfield images were acquired using Nikon Eclipse80i with 60X objective (zoom X1.4) at 400 nm steps in z axis. Sholl, dendritic, and spine analyses were performed using NeuroLucida 360 software (MBF Bioscience). For the analyses, “rostral” was defined as the cortical region from the beginning of the cortex until the beginning of the hippocampus, and “caudal” was defined as the cortical region from the beginning of the hippocampus until the end of the cortex.

### **Mitochondrial morphology analysis**

Mouse neural stem cells were prepared from E15.5 embryos. Dissected cortex was dissociated with papain and resuspended in stem cell culture medium (DMEM with 2% B27, 1% N2, 40 ng/ml bFGF, 1% v/v penicillin-streptomycin, 1% amphotericin B). Cells were plated on poly-L-ornithine/fibronectin-coated glass coverslips and maintained for 2 days. Cells were then treated with 100 nM MitoTracker Red CMXRos (Thermo Fisher Scientific, M7512) for 45 min, washed with warm PBS, and fixed with 4% PFA. Images were acquired on a Zeiss LSM880 with 63X objective at 300 nm steps (~20 steps depending on cell size) in z axis. Images were analyzed using Fiji (4). Images were first preprocessed using a custom macro to subtract background, reduce noise, and enhance local contrast. Mitochondrial morphology was then analyzed using the “Morphometry” macro to measure the average size of mitochondria ( $area^2$ ), length, aspect ratio, form factor, and area-weighted form factor (7).

## Metabolomics profiling

The metabolome was extracted from plasma samples by adding 950  $\mu$ l of ice-cold methanol/water (80% v/v) to 50  $\mu$ l of plasma, followed by rigorous vortexing and centrifugation at  $\sim 20,160 \times g$  for 15 min. For cortical metabolome extraction, 50 mg of tissue was homogenized in 1 ml of methanol/water (80% v/v), 200  $\mu$ l of homogenate was transferred into 800  $\mu$ l of ice-cold methanol/water (80% v/v), followed by rigorous vortexing and centrifugation at  $\sim 20,160 \times g$  for 15 min. The supernatants were then processed, metabolomics profiling was performed, and raw data was analyzed as previously described (8). Data was normalized, and statistical and multivariate analyses were performed using ANOVA and Partial Least Squares Discriminant Analysis (PLS-DA) in MetaboAnalyst version 4.0 with the following settings: normalization by median, log transformation, and data scaling with mean centering (auto scaling).

## Enzymatic activity assays

To detect the oxidative activity of BCKDC in liver, brain, and skeletal muscle of WT and *Ube3b*<sup>-/-</sup> mice, isolated mitochondria from these tissues were analyzed using the Seahorse XFe96 Extracellular Flux Analyzer (Seahorse Bioscience). Liver, brain, and skeletal tissues were lysed in mitochondria isolation buffer (MIB) (10 mM HEPES, 220 mM mannitol, 70 mM sucrose, 1 mM EGTA pH7.4) supplemented with cComplete mini EDTA-free protease inhibitor and phosSTOP phosphatase inhibitor tablets (Roche). Lysates were clarified with three spins at  $600 \times g$  for 5 min at 4°C. Heavy membranes (containing mitochondria) were collected at  $10,000 \times g$  for 10 min at 4°C, followed by three washes with MIB. The final pellets were gently resuspended in MIB. Protein concentrations were determined using the BCA protein assay. Oxygen consumption rate (OCR) measurements were performed using the Seahorse XFe96 Extracellular Flux Analyzer (Seahorse Bioscience). Mitochondria were plated at 10  $\mu$ g protein per well in 25  $\mu$ l volume, and pelleted at  $2700 \times g$  for 5 min. Experimental buffer (EB) (125  $\mu$ l per well; 10 mM HEPES, 125 mM KCl, 2 mM MgCl<sub>2</sub>, 0.1 mM EGTA, 5 mM K<sub>2</sub>HPO<sub>4</sub>), either with no supplement, or supplemented with 5 mM succinate, or 5 mM  $\alpha$ -ketoisovaleric acid ( $\alpha$ -KIV) and 0.4 mM coenzyme A (CoA) was added to each well. The assay was run with sequential injections of ADP (final concentration: 4 mM), antimycin A (final concentration: 2  $\mu$ M). Each measurement cycle consisted of a mixing time of 3 min and a data acquisition period of 3 min. Each datum was determined minimally in triplicate. The baseline OCR after antimycin A injection was subtracted from the highest observed state 3 respiration (following ADP injection). Substrate-induced respiration was calculated from the OCR difference between wells with EB and EB plus  $\alpha$ -KIV and CoA. The resulting OCR stimulation was normalized to the amount of protein per well.

## Tissue preparation

After anesthetizing mice with a ketamine/xylazine cocktail, the animals were perfused with cold 1X PBS for 3 min followed by cold 4% PFA in PBS for 15 min at a rate of 7 ml/min. Brains were dissected out and gently rinsed with cold 1X PBS, followed by incubation in PFA overnight at 4°C. Fixed brains were cryoprotected by incubation in an increasing concentration gradient of sucrose, starting in 5% and ending in 25% sucrose solution. Brains were embedded in OCT and sectioned at 50  $\mu$ m thickness on a cryostat (Leica CM3050s).

### **$\beta$ -galactosidase staining**

Tissue sections were washed with cold 1X PBS, followed by incubation in 1 mg/ml X-gal (5-bromo-4-chloro-3-indolyl  $\beta$ -D-galactopyranoside) staining solution (5 mM  $K_3Fe(CN)_6$ , 5 mM  $K_4Fe(CN)_6$ , 2 mM  $MgCl_2$ , 0.02% Igepal CA-630, 0.01% sodium deoxycholate), at 37°C overnight. Sections were transferred onto slides, then incubated in an increasing gradient of 50%, 75%, 90%, and 100% ethanol for 1 min each. Slides were then immersed in xylene five times and mounted with Permount mounting media (Fisher). The images were acquired using a Nikon Eclipse 80i microscope with a DS-Ri1 color camera (Nikon) at 4X magnification.

### **Nissl staining**

Sagittal sections were loaded on 3% gelatin-coated glass slides. Dried sections were dehydrated with 70%, 95%, and 100% ethanol and rehydrated with 95%, 70%, and 50% ethanol and distilled water. Sections were stained with 0.5% cresyl violet solution for 30 min, cleared with 70%, 95%, and 100% ethanol and xylene and mounted with Cytoseal (Thermo Fisher Scientific). Images were scanned with an Axioscan Z1 (Zeiss) with 20X objective. WT and knockout sagittal brain sections were matched based on hippocampal structure, and corpus callosum area, ventricle area, and cortical thickness were measured in ZEN Blue edition (Zeiss). Cortical thickness was measured from the outer layer of the cerebral cortex to the corpus callosum.

### **Behavioral assays**

All mice were age- and sex-matched littermate progeny of heterozygous *Ube3b* mutant crosses. An experimenter blind to genotypes performed all behavioral tests. Mice were tested at 5-8 weeks of age except where indicated, and tests were performed in the order in which they appear below.

**Ultrasonic vocalization.** Ultrasonic vocalizations (USVs) were recorded at P4 and P9 for both male and female pups isolated from their mothers during the daylight period of the light/dark cycle. Dams and their litters were acclimated to the test room for 30 min. Each pup was removed from the cage containing its mother and littermates and placed in a clean plastic container in a wooden sound-attenuating recording chamber. Each pup was first acclimated to the recording chamber for 30 seconds (sec) then recorded for 10 min. Recordings were acquired using an UltraSoundGate CM16/CMPA condenser microphone (Avisoft Bioacoustics) positioned at a fixed height of 8 cm above the pups, and were amplified and digitized (sampled at 16 bits, 250 kHz) using UltraSoundGate 416 hr 1.1 hardware and Avisoft-RECORDER software (Avisoft Bioacoustics). The data were transferred to Avisoft-SASLab Pro (version 5.2) to analyze spectrograms of vocalizations with settings of 0% overlapping FlatTop windows, 100% frame size, and 256 points fast Fourier transform (FFT) length. The following measures were recorded and analyzed for each group: number of USV calls, mean duration of USV calls, mean amplitude, mean peak frequency, mean interval between USV calls, and the latency to call.

**Self-grooming.** Mice were placed into a new standard cage, without nestlets, food, or water, acclimated for 10 min, then videotaped for another 10 min. The amount of time spent grooming was recorded continuously to

calculate the total time spent grooming. Grooming was considered self-grooming of any part of the body (including the face, head, ears, body, or tail). Data was plotted as percent of total time spent grooming.

**Marble burying.** The test mouse was acclimated to the test room for 30 min. One standard housing cage for each test mouse was filled with clean bedding material. Fifteen clean marbles were arranged on top of the bedding in each cage, forming five even rows and three columns. Mice were placed individually into the prepared cages and kept undisturbed for 30 min. After the testing period, they were returned to their original cages. A still image of the test cage was taken to record the number of buried marbles. A marble was considered buried if more than two-thirds of its depth is covered. Results were plotted as the total number of marbles buried per genotype.

**Nest building.** Test mice were single-housed in their home cages right before the dark phase, and one nestlet was placed in each cage on day 1. At the beginning of the light phase on the next day (12 hr time point), the quality of the nest was examined, and the nest was photographed. The nest quality was subsequently assessed at 24 hr, 36 hr, 48 hr, and 60 hr time points. Nest quality was scored on a scale of 0 to 3 at each time point (0 being no nest construction, 3 being a well-structured nest) (Fig. S3D).

**Grip strength test.** Muscle strength was measured by a grip strength test performed by the Neuro-Models Core Facility at UTSW in a blinded fashion. The test was conducted using a wire mesh grid connected to a horizontally-aligned force meter (San Diego Instruments). The grid was secured at a 45-degree angle, and the top rung of the grid was used for all testing. Mice were held at the base of the tail and supported ventrally while being moved into position to grasp the wire grid. Once the rung was successfully grasped, mice were gently pulled in a horizontal plane until their grip was released from the grid. Peak force (in gram-force units) was captured and recorded by the force meter. The forelimbs and hindlimbs were tested separately, with each measured six times over a 2 min period.

### **Statistical analyses**

All statistical analyses were performed using GraphPad Prism ([www.graphpad.com/scientific-software/prism](http://www.graphpad.com/scientific-software/prism), RRID: SCR\_002798). All analyses were performed using at least 3 different animals of each genotype or 3 replicates for cell lines. Data are represented as mean  $\pm$  SEM and two-tailed p-values are reported. GraphPad Prism was used to perform either one-way (factor: genotype) or two-way (factors: genotype and age or time) ANOVA with Tukey's multiple comparisons test, or unpaired t test where applicable. Images were processed with Adobe Photoshop ([www.adobe.com/products/photoshop](http://www.adobe.com/products/photoshop), RRID: SCR\_014199) and quantified using ImageJ ([rsb.info.nih.gov/ij/index.html](http://rsb.info.nih.gov/ij/index.html), RRID: SCR\_003070), Fiji ([fiji.sc](http://fiji.sc), RRID: SCR\_002285), ZEN Blue edition ([www.zeiss.com/microscopy/us/products/microscope-software/zen-lite](http://www.zeiss.com/microscopy/us/products/microscope-software/zen-lite), RRID: SCR\_013672), or NeuroLucida 360 ([www.mbfioscience.com/neuroLucida360](http://www.mbfioscience.com/neuroLucida360), RRID: SCR\_001775) where applicable. All figures were prepared using Adobe Illustrator ([www.adobe.com/products/illustrator](http://www.adobe.com/products/illustrator), RRID: SCR\_010279).

**Electronic resources**

Allen Brain Atlas: <http://www.brain-map.org>

gnomAD Browser: <http://gnomad.broadinstitute.org>

GTEx Portal: <https://www.gtexportal.org/home>

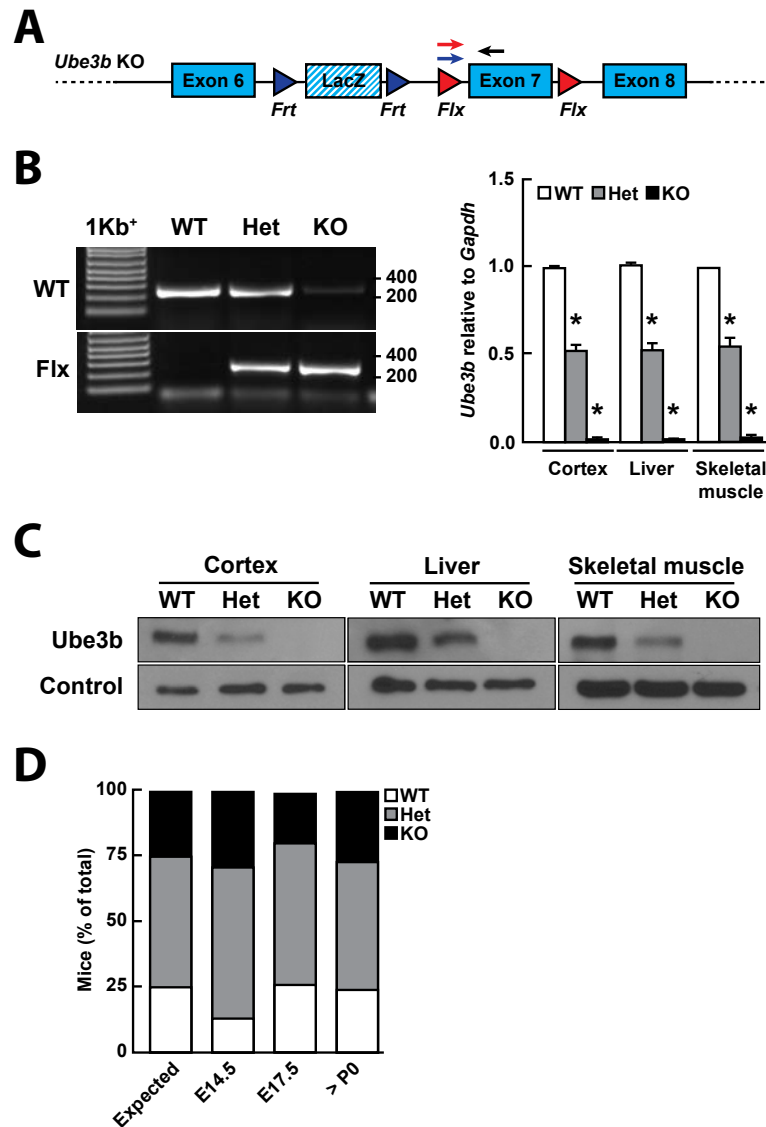
KEGG: <http://www.genome.jp/kegg>

MetaboAnalyst: <http://www.metaboanalyst.ca/MetaboAnalyst/faces/home.xhtml>

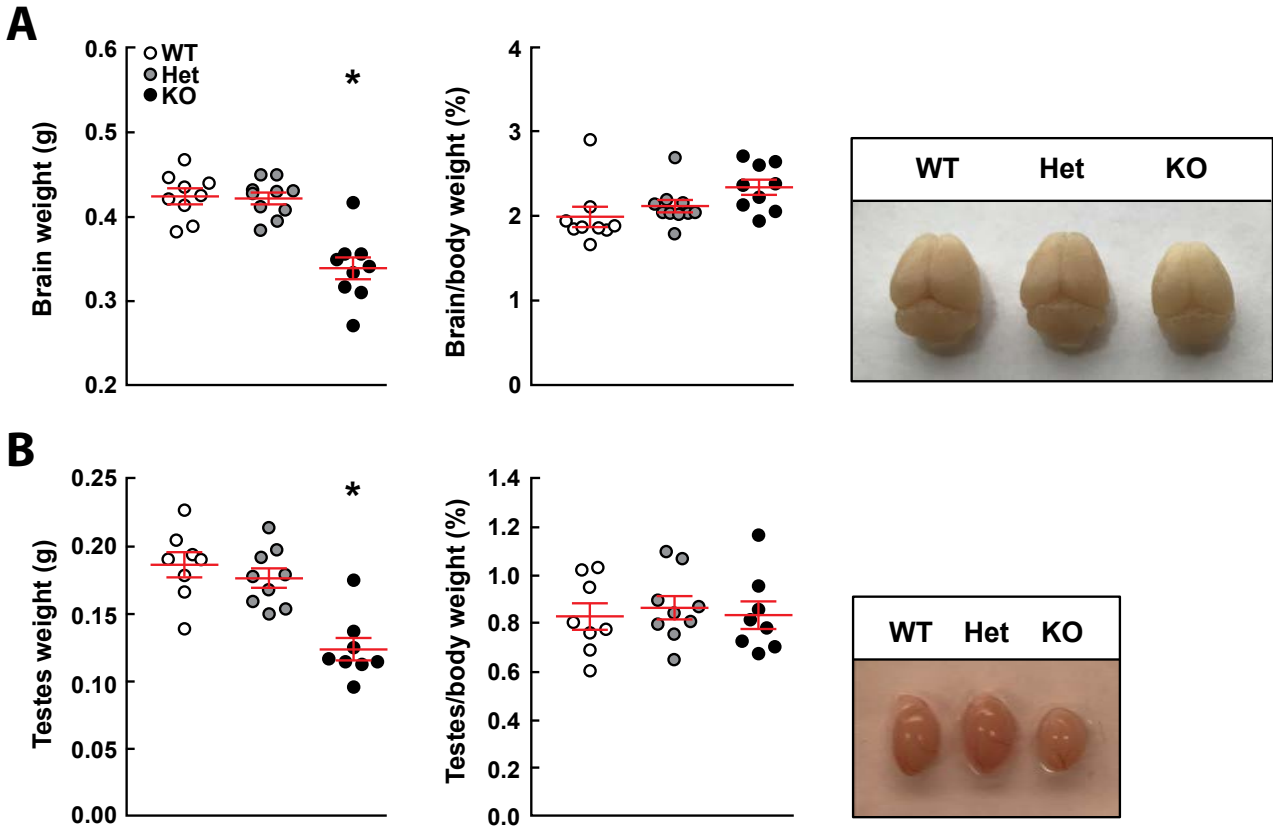
OMIM: <http://www.omim.org>

UCSC Genome Browser: <http://genome.ucsc.edu>

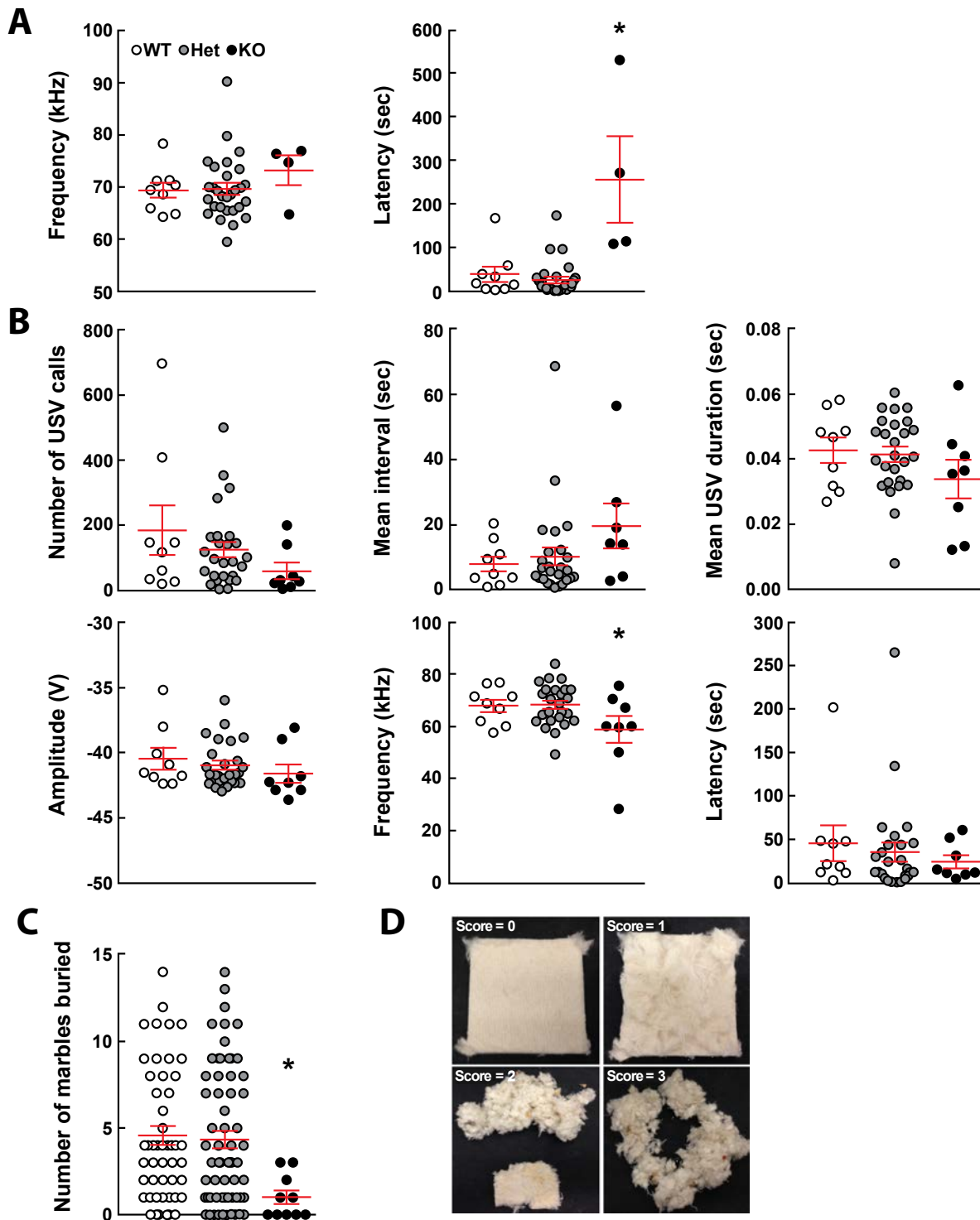
## Supplementary Figures



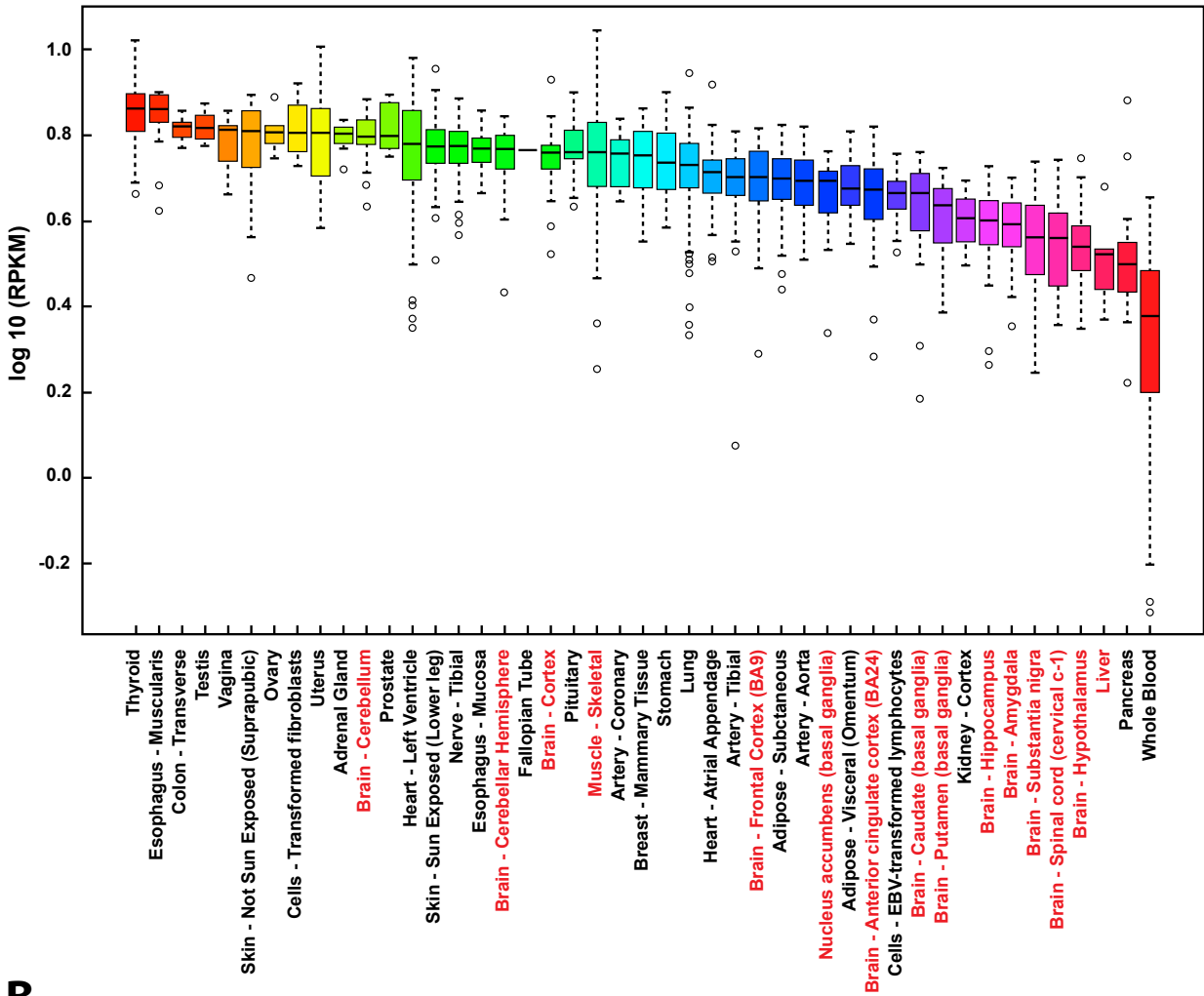
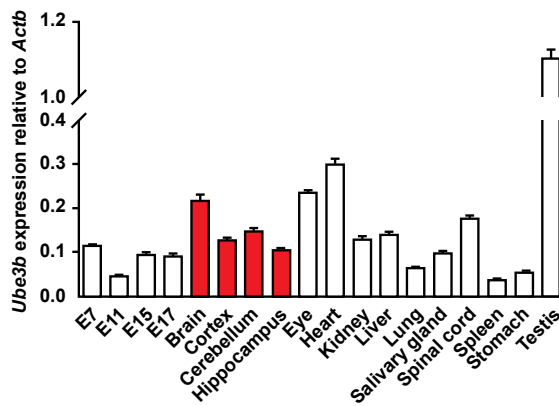
**Fig. S1. Generation of the *Ube3b* constitutive knockout mouse model.** (A) Schematic of the targeted *Ube3b* locus disrupting exon 7 and resulting in loss of Ube3b. Arrows represent locations of genotyping primers (red: WT allele forward primer, blue: KO allele forward primer, black: reverse primer common to both alleles). (B) Genotyping strategy (*left*) and qRT-PCR analysis (*right*) of total RNA from cortex, liver, or skeletal muscle in WT, *Ube3b*<sup>+/-</sup> (Het), or *Ube3b*<sup>-/-</sup> (KO) showed a ~50% decrease in *Ube3b* expression in the Het and complete loss of expression in the KO compared to WT (\**P*<0.0001, one-way ANOVA). Values are mean ± SEM from three independent experiments, each performed in triplicate. (C) Western blot analysis from cortex, liver, or skeletal muscle tissue from WT, Het, or KO confirmed loss of Ube3b protein in the KO. Control refers to immunoblotting with anti-actin (cortex) or anti-GAPDH (liver and skeletal muscle). (D) KO mice are born in expected Mendelian ratios (data from 3-9 litters per age group). The number of mice born from each genotype was not significantly different from the number of expected mice based on Mendelian ratios ( $\chi^2$  test, embryonic day (E)14.5: *P*=0.0964, E17.5: *P*=0.6106, > postnatal day (P)0: *P*=0.9477).



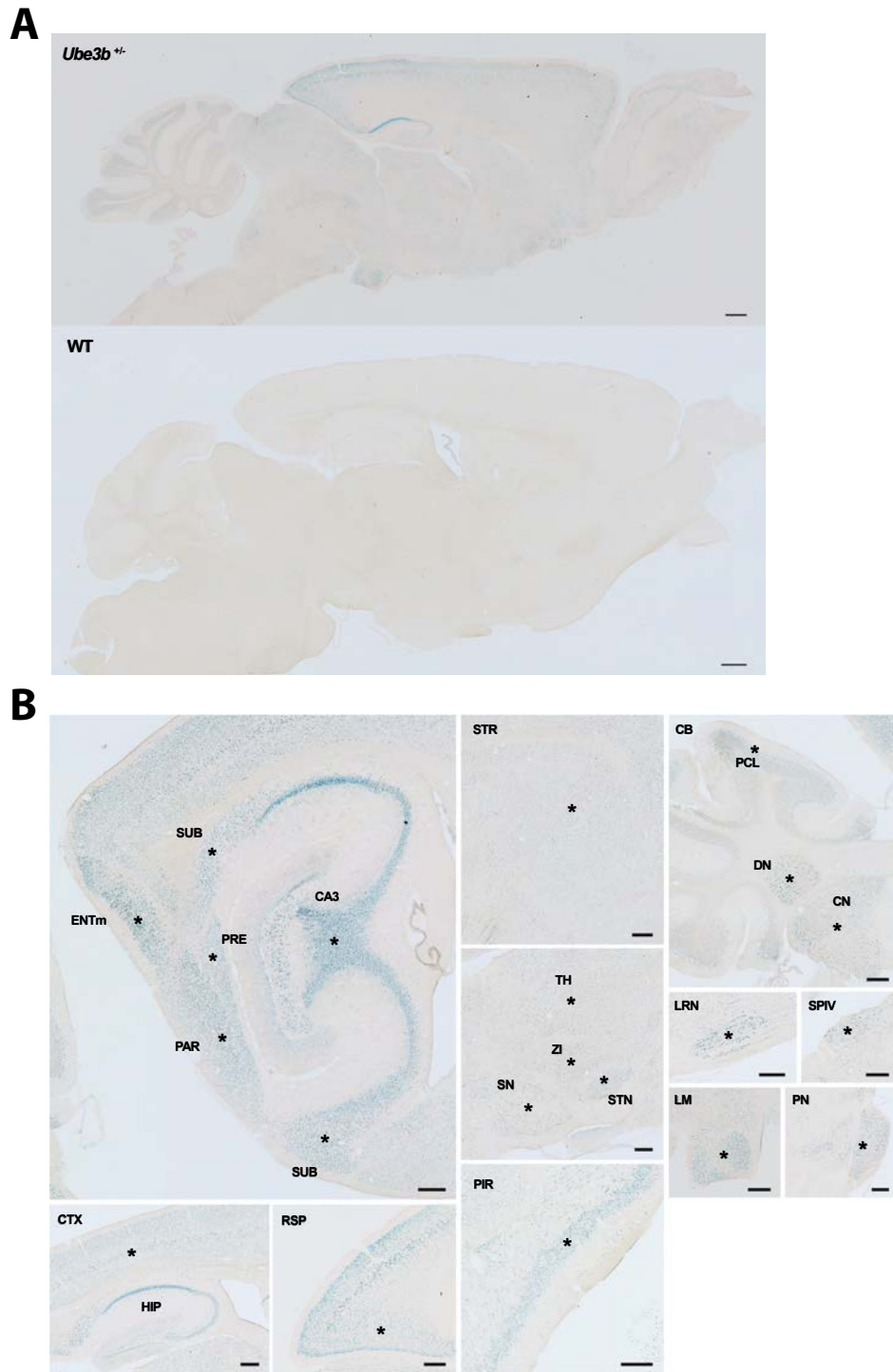
**Fig. S2. Reduced brain and testes weight of the *Ube3b* KO mice.** Brain (A) and testes (B) weights were measured at 9 weeks of age ( $*P < 0.0001$ , one-way ANOVA,  $n = 8-9$  WT,  $9-10$  Het,  $8-9$  KO). Representative images of brains and testes from WT, Het, and KO are shown. Values are mean  $\pm$  SEM.



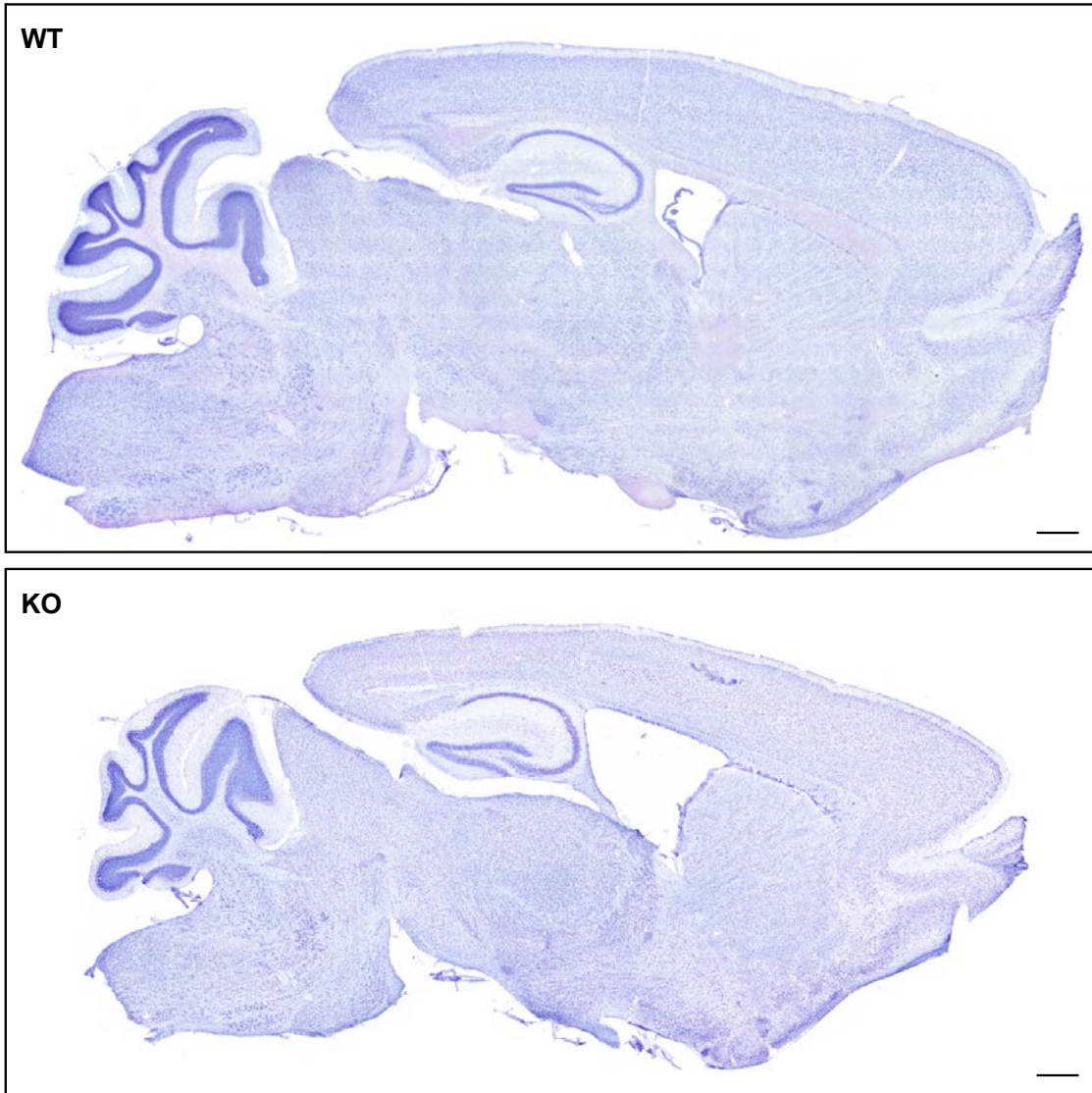
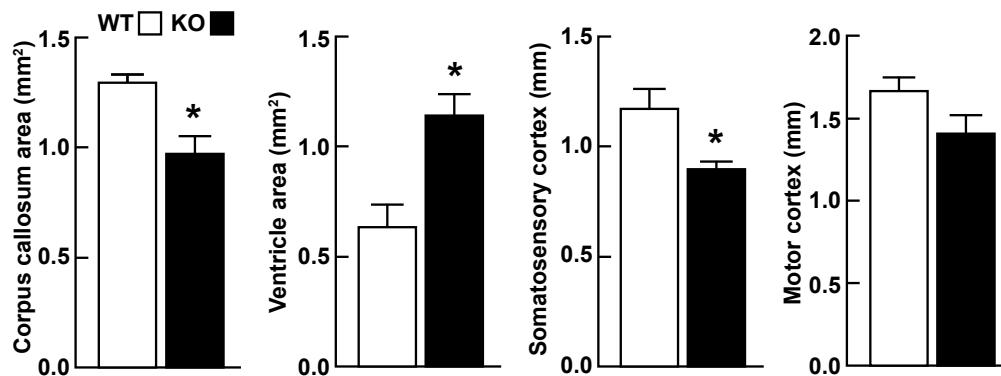
**Fig. S3. *Ube3b* KO mice show impaired ultrasonic vocalizations and marble burying.** (A) Mean peak frequency of USVs and latency to call measured at P4 (mean peak frequency: n=9 WT, 29 Het, 4 KO; latency to call: \* $P < 0.0001$ , n=9 WT, 29 Het, 4 KO). (B) Altered mean peak frequency of USVs at P9 (number of USVs: n=9 WT, 26 Het, 8 KO; mean interval: n=9 WT, 26 Het, 7 KO; mean USV duration: n=9 WT, 26 Het, 8 KO; mean peak amplitude: n=9 WT, 26 Het, 8 KO; mean peak frequency: \* $P = 0.0385$ , n=9 WT, 26 Het, 8 KO; latency to call: n=9 WT, 26 Het, 8 KO). (C) KO mice do not bury as many marbles as their WT or Het littermate controls (\* $P = 0.0254$ , n=49 WT, 63 Het, 10 KO). (D) Nest scoring, with 0 being no nest construction to 3 being a well-structured nest.

**A****B**

**Fig. S4. *Ube3b* is ubiquitously expressed across tissues.** (A) *Ube3b* human tissue expression data publicly available from GTEx (Genotype-Tissue Expression Portal). (B) qRT-PCR analysis of total RNA from mouse tissue. Values are mean  $\pm$  SEM from three independent experiments, each performed in triplicate.



**Fig. S5.  $\beta$ -galactosidase staining reveals *Ube3b* promoter activity in a neuronal pattern throughout the brain.** *Ube3b* promoter activity via  $\beta$ -galactosidase staining. (A) Overview of *Ube3b* expression throughout the brain. (B) Brain regions are annotated based on the Allen Brain Atlas adult mouse brain reference atlas. Labeled regions are indicated by an asterisk. CA3, field CA3 of the hippocampus, CB, cerebellum, CN, cochlear nuclei, CTX, cortex (\* layer V), DN, dentate nucleus, ENTm, medial entorhinal area, HIP, hippocampus, LM, lateral mammillary nucleus, LRN, lateral reticular nucleus, PAR, parasubiculum, PCL, Purkinje cell layer, PIR, piriform cortex, PN, pontine nuclei, PRE, presubiculum, RSP, retrosplenial area, SN, substantia nigra, SPIV, spinal vestibular nucleus, STN, subthalamic nucleus, STR, striatum, SUB, subiculum, TH, thalamus, ZI, zona incerta. Scale bars, 250  $\mu$ m.

**A****B**

**Fig. S6. Neuroanatomical abnormalities in the *Ube3b* KO mice.** Nissl staining of brains from *Ube3b*<sup>-/-</sup> and WT mice revealed a hypoplastic corpus callosum, enlarged ventricles, and decreased thickness of the primary somatosensory cortex in the KO compared to WT. The thickness of the primary motor cortex was not different. Representative images of Nissl stained brains (A) and quantification of the abnormalities (B) are shown (corpus callosum area: \**P*=0.0153, ventricle area: \**P*=0.0196, thickness of the somatosensory cortex: \**P*=0.0376, *n*=3 WT, 3 KO). Scale bars, 500  $\mu$ m.

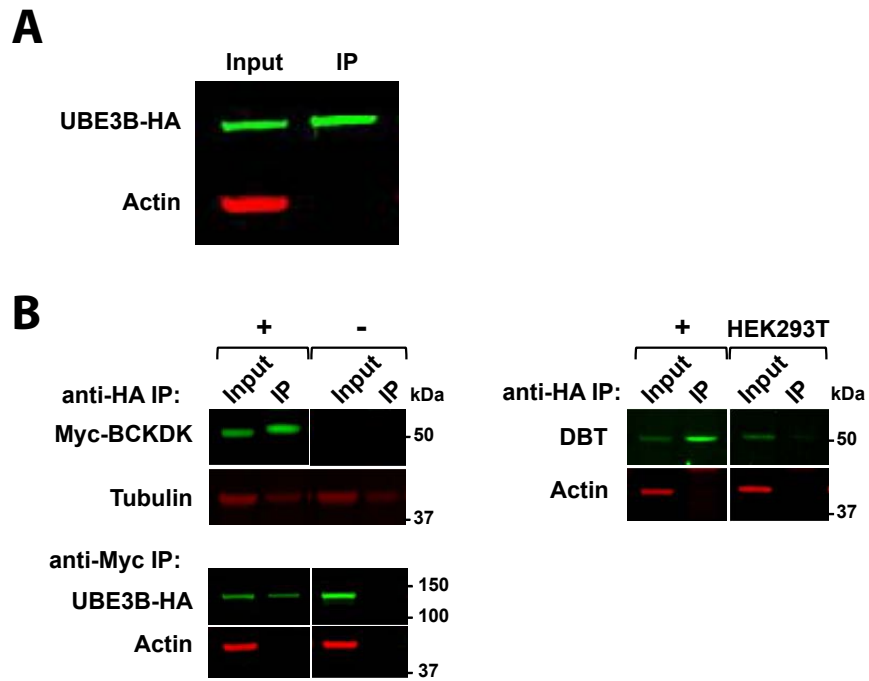


**Fig. S7. UBE3B interacts with BCKDK and DBT.** (A) Immunoprecipitation (IP) of UBE3B-HA from stable HEK293T cells. (B) (*left*) HEK293T stable cells expressing UBE3B-HA (HEK293T-UBE3B) were transfected with Myc-BCKDK (+) or empty vector (-). Lysates were immunoprecipitated (IP) with anti-HA (*top*) or anti-Myc (*bottom*) agarose, and starting material (Input) and IP fractions were analyzed by anti-Myc (*top*) or anti-HA (*bottom*) immunoblotting. (*right*) Lysates from HEK293T-UBE3B (+) or HEK293T cells were immunoprecipitated using anti-HA agarose and Input and IP fractions were analyzed by anti-DBT immunoblotting.

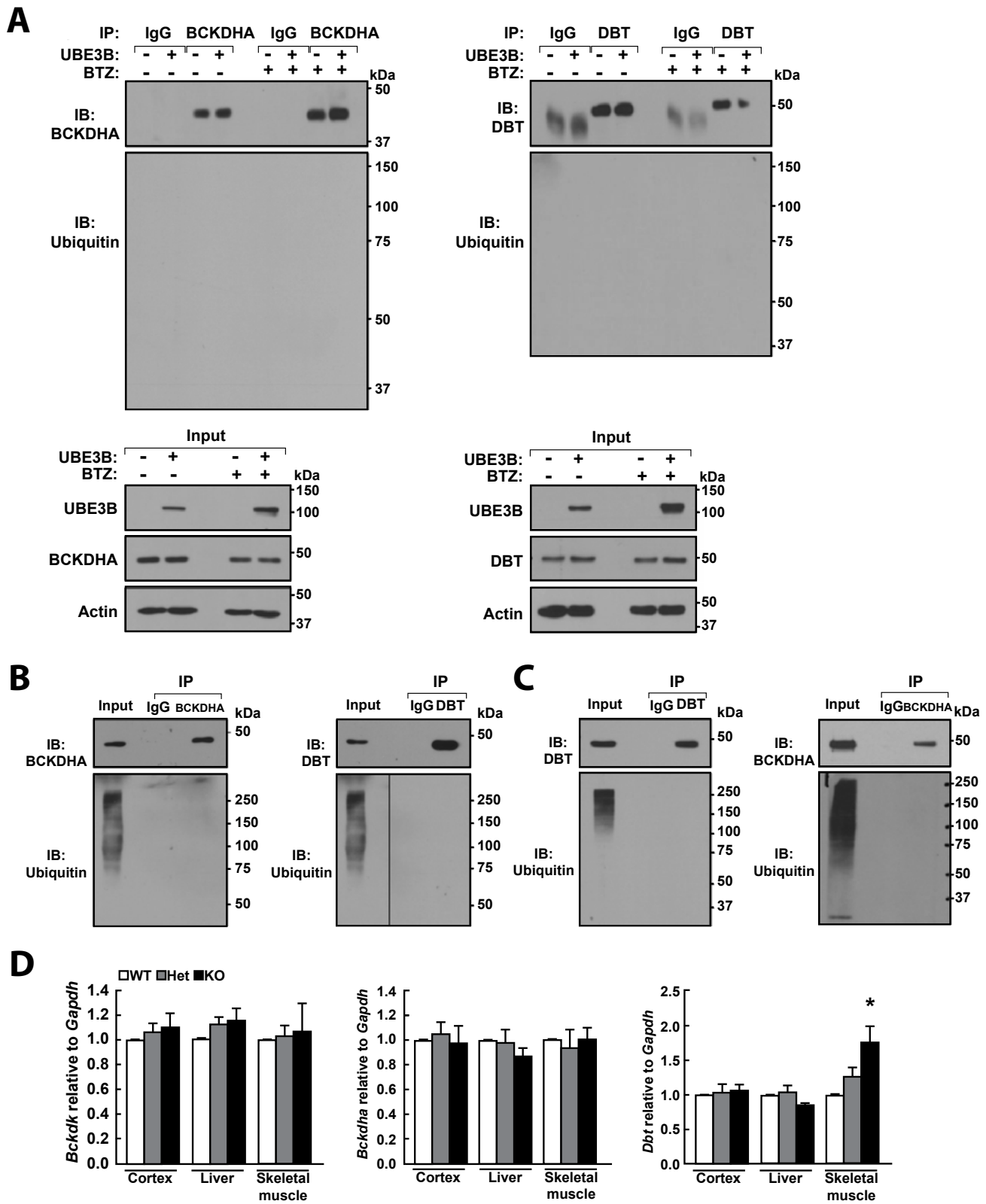


**Fig. S8. Ube3b does not ubiquitinate BCKDHA or DBT.** (A) HEK293T (-) or HEK293T-UBE3B (+) cells were treated with Bortezomib (BTZ) (+) or vehicle (-). Lysates were subject to denaturing immunoprecipitation (IP) with anti-BCKDHA, anti-DBT, or IgG agarose. IP fractions were analyzed by anti-BCKDHA, anti-DBT, or anti-ubiquitin immunoblotting (IB). Starting material (Input) fractions were analyzed by anti-Ube3b, anti-BCKDHA, anti-DBT, or anti-actin IB. Lysates from cortex (B) or liver (C) tissue of WT mice were subject to denaturing IP with anti-BCKDHA, anti-DBT, or IgG agarose. Starting material (Input) and IP fractions were analyzed by anti-

BCKDHA, anti-DBT, or anti-ubiquitin immunoblotting (IB). (D) qRT-PCR analysis of total RNA from cortex, liver, or skeletal muscle tissue of WT, Het, or KO showed no changes in *Bckdk* or *Bckdha* expression in all tissues and an upregulation of *Dbt* expression only in skeletal muscle (*Dbt*: skeletal muscle \* $P=0.0137$ ; for each tissue  $n=3-4$  WT, 3-4 Het, 3-4 KO). Values are mean  $\pm$  SEM from three independent experiments, each performed in triplicate.

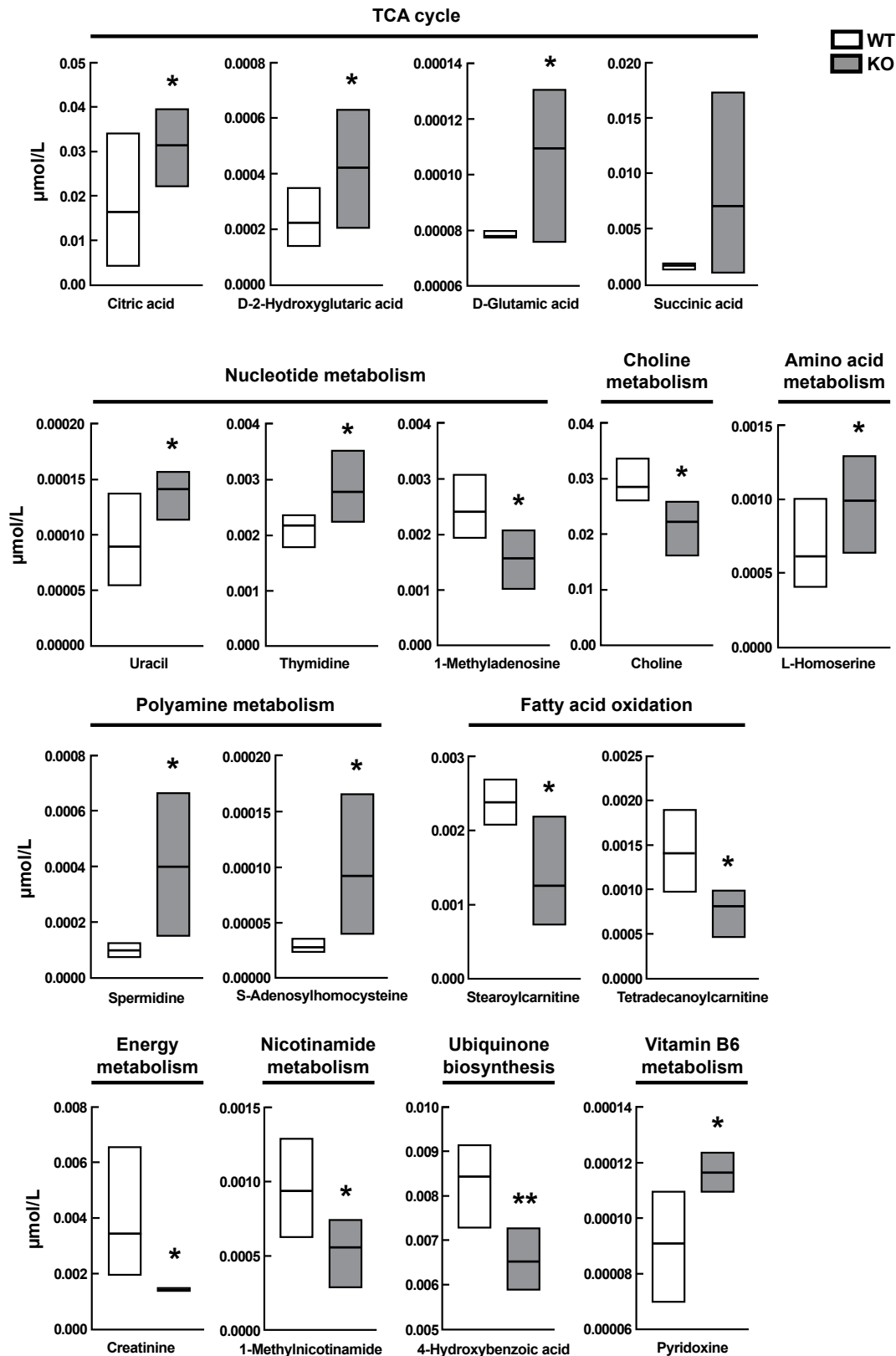


**Fig. S9. Metabolites that were most significantly altered in plasma from *Ube3b* KO mice.** Metabolites most significantly altered in *Ube3b* KO plasma compared to WT plasma were from the TCA cycle, fatty acid oxidation, ubiquinone biosynthesis, nucleotide, choline, amino acid, polyamine, energy, nicotinamide, and vitamin B6 metabolism (\*\* $P < 0.005$ , \* $P < 0.05$ ,  $n = 5$  WT, 5 KO). The line within each box represents the mean and the box boundaries represent minimum and maximum values.

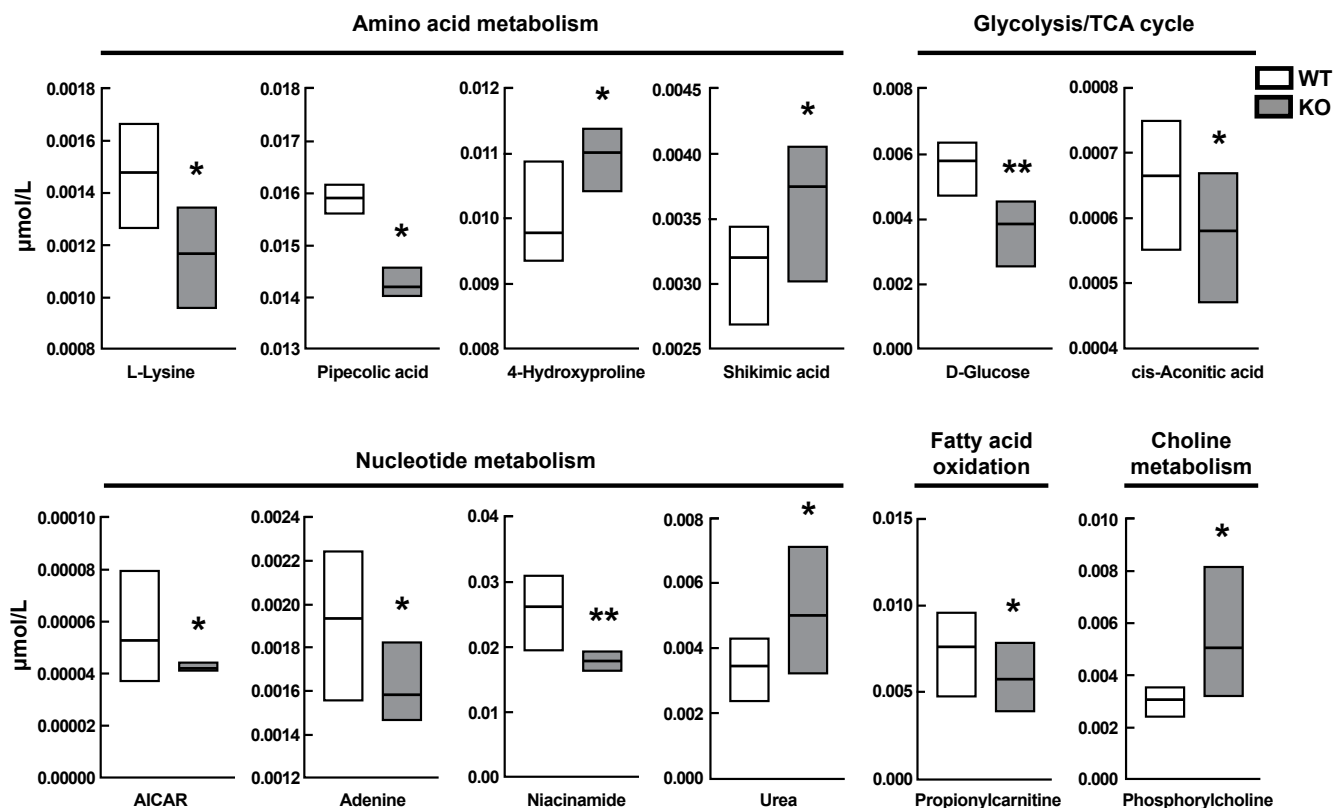


**Fig. S10. Metabolites that were most significantly altered in cortex from *Ube3b* KO mice.** Metabolites most significantly altered in *Ube3b* KO cortex compared to WT cortex were from the amino acid and nucleotide metabolism, glycolysis/TCA cycle, fatty acid oxidation, and choline metabolism (\*\* $P < 0.005$ , \* $P < 0.05$ ,  $n = 6$  WT, 6 KO). The line within each box represents the mean and the box boundaries represent minimum and maximum values.

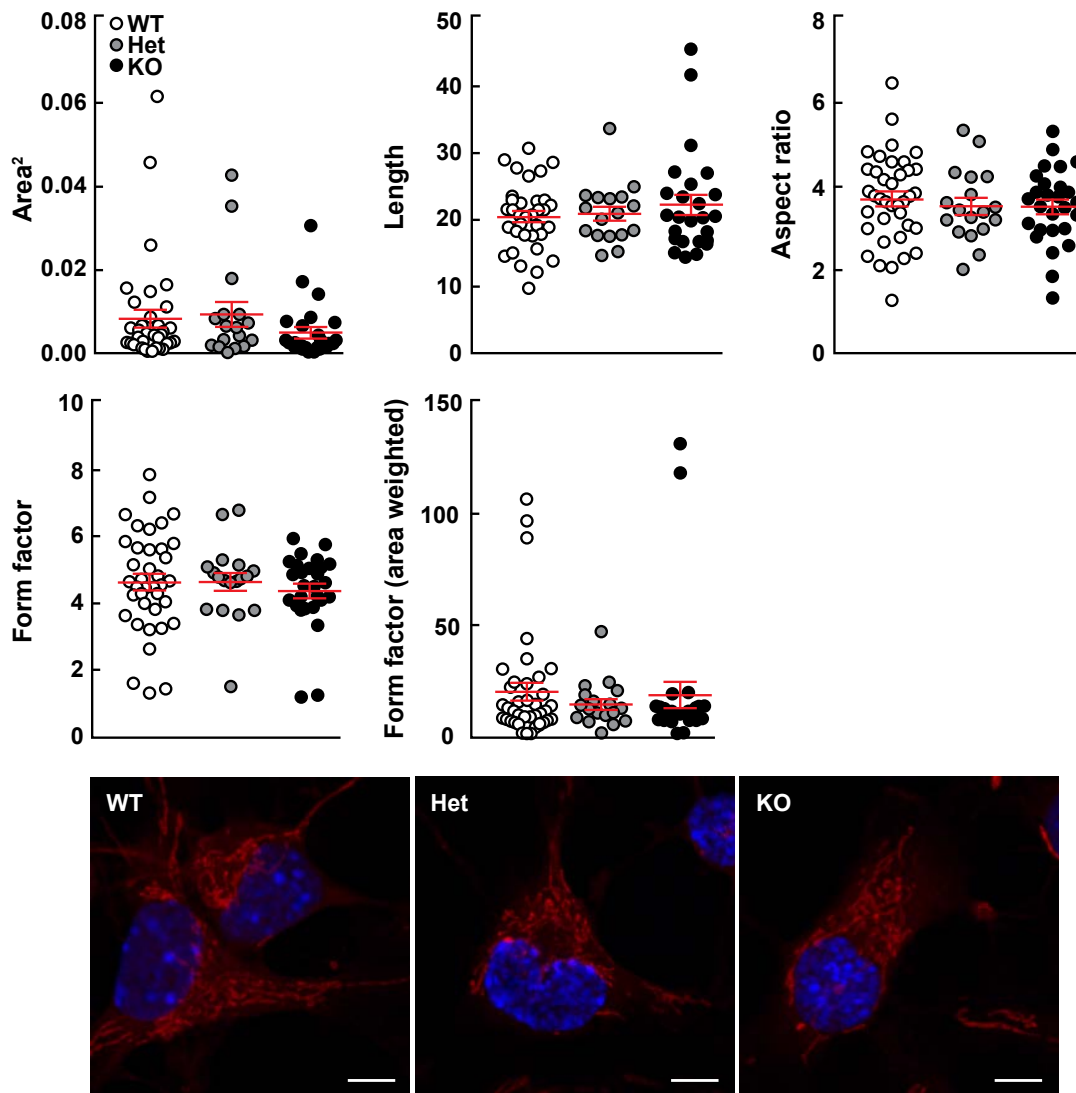


**Fig. S11. Loss of *Ube3b* did not affect mitochondrial morphology.** Analysis of mitochondrial morphology did not reveal any abnormalities in mitochondria from KO neural stem cells compared to those from WT or Het cells (n=35-38 WT, 17-18 Het, 25-27 KO). Scale bars, 5  $\mu$ m.

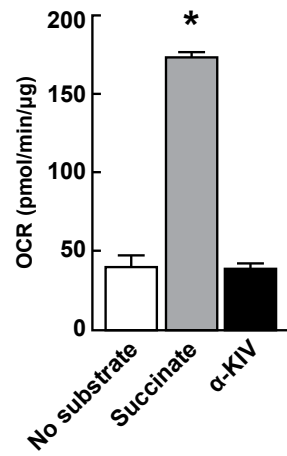


**Fig. S12. BCKDC activity was not detected in brain mitochondria.** Mitochondrial respiration was measured from WT brain. There was no detectable  $\alpha$ -KIV-induced respiration compared to no substrate ( $P=0.9607$ ,  $n=3$ ). Succinate was used as a positive control ( $*P<0.0001$ ,  $n=3$ ). Values are mean  $\pm$  SEM.

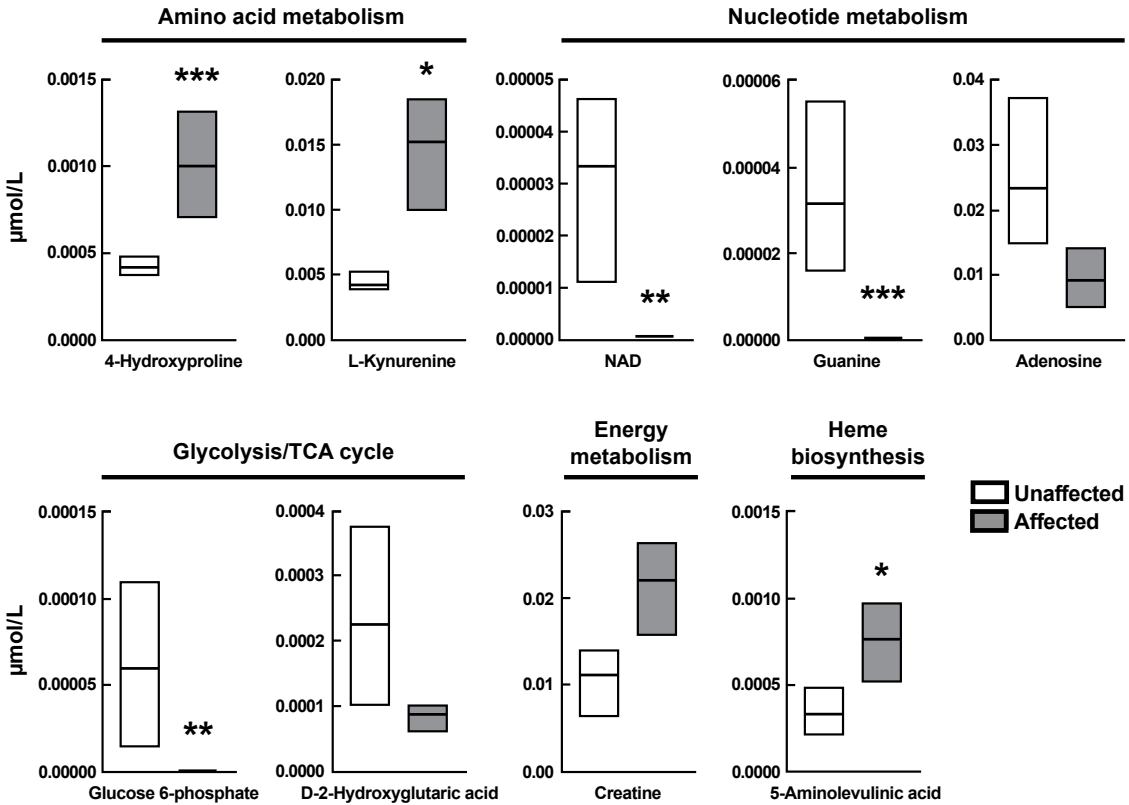


**Fig. S13. Metabolites that were most significantly altered in plasma from KOS patients.** Metabolites most significantly altered in plasma from KOS patients compared to plasma from unaffected individuals were from the amino acid and nucleotide metabolism, glycolysis/TCA cycle, energy metabolism, and heme biosynthesis (\*\*\* $P \leq 0.0008$ , \*\* $P < 0.005$ , \* $P < 0.05$ ,  $n = 3$  unaffected, 3 affected). The line within each box represents the mean and the box boundaries represent minimum and maximum values.

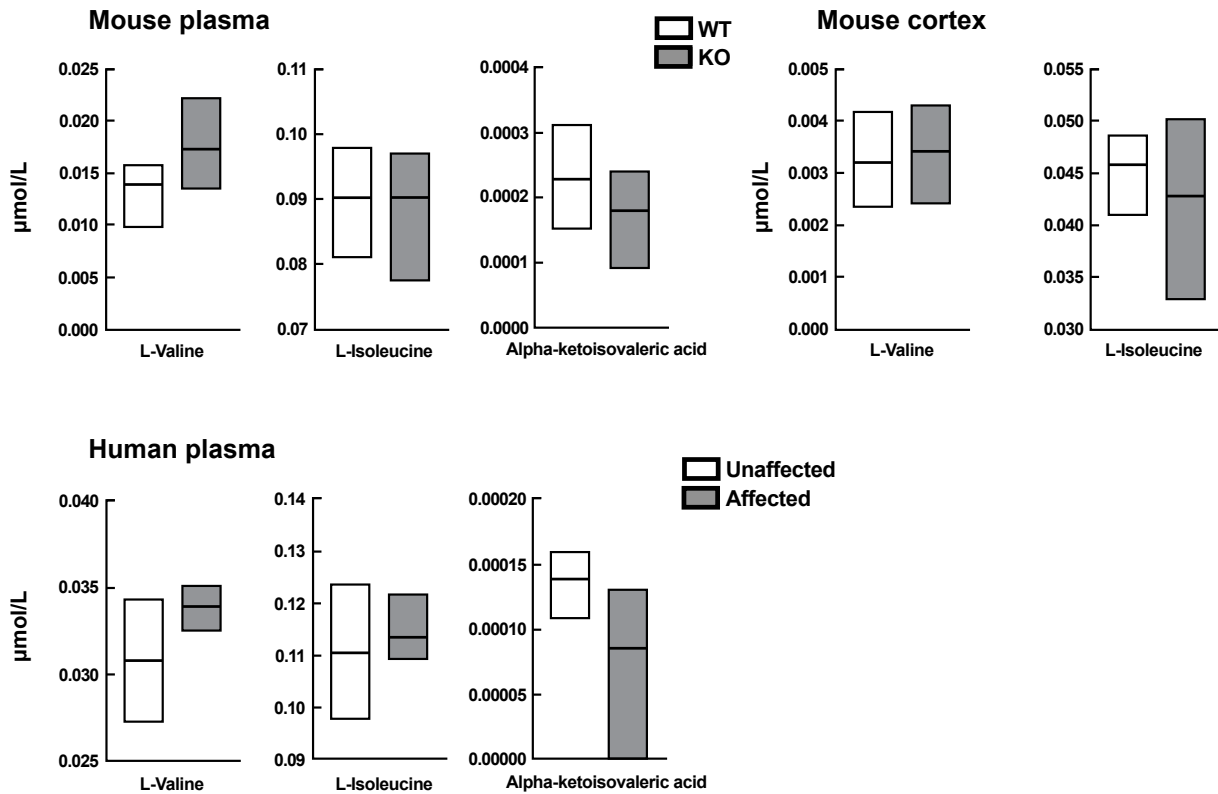


**Fig. S14. Levels of metabolites from the BCAA metabolism pathway.** Metabolites from the BCAA pathway were not significantly altered in plasma or cortex from *Ube3b* KO compared to WT mice, or from plasma of KOS patients compared to unaffected individuals. The line within each box represents the mean and the box boundaries represent minimum and maximum values.

## Supplementary Datasets

**Dataset S1.** The list of 204 metabolites profiled in plasma and cortical tissue samples. Metabolites, their transitions ( $m/z$ ), declustering potentials (DP, in Volts), and collision energies (CE, in Volts) are reported. Q1, quadrupole 1, Q3, quadrupole 3, DP, declustering potential, CE, collision energy, CXP, collision cell exit potential, RT, retention time. Alternative pathway names are indicated in parentheses.

**Dataset S2.** The relative abundance of metabolites detected from *Ube3b*<sup>-/-</sup> and WT plasma (A), *Ube3b*<sup>-/-</sup> and WT cortex (B), and plasma samples from affected and unaffected individuals (C). Relative abundance was calculated by normalizing the peak areas to the protein content (mg) of each sample. Fold changes and *P* values were calculated using MetaboAnalyst. VIP values  $\geq 1$  are highlighted. Avg, average, SD, standard deviation, VIP, variable importance in projection.

## References

1. Rappsilber J, Mann M, & Ishihama Y (2007) Protocol for micro-purification, enrichment, pre-fractionation and storage of peptides for proteomics using StageTips. *Nature protocols* 2(8):1896-1906.
2. Sowa ME, Bennett EJ, Gygi SP, & Harper JW (2009) Defining the human deubiquitinating enzyme interaction landscape. *Cell* 138(2):389-403.
3. Schneider CA, Rasband WS, & Eliceiri KW (2012) NIH Image to ImageJ: 25 years of image analysis. *Nature Methods* 9(7):671-675.
4. Schindelin J, *et al.* (2012) Fiji: an open-source platform for biological-image analysis. *Nature Methods* 9(7):676-682.
5. Chanaday N (2018) Synapse-Count-macro-for-Fiji. *GitHub* <https://github.com/nchanaday/Synapse-Count-macro-for-Fiji>.
6. Zaqout S & Kaindl AM (2016) Golgi-Cox Staining Step by Step. *Front Neuroanat* 10:38.
7. Merrill RA, Flippo KH, & Strack S (2017) Measuring Mitochondrial Shape with ImageJ. *Techniques to Investigate Mitochondrial Function in Neurons*, ed Strack S (Humana Press, New York, NY), Vol 123, pp 31-48.
8. Mullen AR, *et al.* (2014) Oxidation of alpha-ketoglutarate is required for reductive carboxylation in cancer cells with mitochondrial defects. *Cell Reports* 7(5):1679-1690.